J. Fluid Mech. (1995), *vol.* 284, *pp.* 97–135

Accelerated flows past a rigid sphere or a spherical bubble. Part 1. Steady straining flow

By JACQUES MAGNAUDET, MAYELA RIVERO† AND JEAN FABRE

Institut de Mécanique des Fluides de Toulouse, URA CNRS 005, Avenue Camille Soula, 31400 Toulouse, France

(Received 31 December 1993 and in revised form 10 May 1994)

This work reports the first part of a series of numerical simulations carried out in order to improve knowledge of the forces acting on a sphere embedded in accelerated flows at finite Reynolds number, *Re*. Among these forces added mass and history effects are particularly important in order to determine accurately particle and bubble trajectories in real flows. To compute these hydrodynamic forces and more generally to study spatially or temporally accelerated flows around a sphere, the full Navier–Stokes equations expressed in velocity–pressure variables are solved by using a finite-volume approach. Computations are carried out over the range $0.1 \leqslant Re \leqslant 300$ for flows around both a rigid sphere and an inviscid spherical bubble, and a systematic comparison of the flows around these two kinds of bodies is presented.

Steady uniform flow is first considered in order to test the accuracy of the simulations and to serve as a reference case for comparing with accelerated situations. Axisymmetric straining flow which constitutes the simplest spatially accelerated flow in which a sphere can be embedded is then studied. It is shown that owing to the viscous boundary condition on the body as well as to vorticity transport properties, the presence of the strain modifies deeply the distribution of vorticity around the sphere. This modification has spectacular consequences in the case of a rigid sphere because it influences strongly the conditions under which separation occurs as well as the characteristics of the separated region. Another very original feature of the axisymmetric straining flow lies in the vortex-stretching mechanism existing in this situation. In a converging flow this mechanism acts to reduce vorticity in the wake of the sphere. In contrast when the flow is divergent, vorticity produced at the surface of the sphere tends to grow indefinitely as it is transported downstream. It is shown that in the case where such a diverging flow extends to infinity a Kelvin–Helmholtz instability may occur in the wake.

Computations of the hydrodynamic force show that the effects of the strain increase rapidly with the Reynolds number. At high Reynolds numbers the total drag is dramatically modified and the evaluation of the pressure contribution shows that the sphere undergoes an added mass force whose coefficient remains the same as in inviscid flow or in creeping flow, i.e. $C_M = \frac{1}{2}$, whatever the Reynolds number. Changes found in vorticity distribution around the rigid sphere also affect the viscous drag, which is markedly increased (resp. decreased) in converging (resp. diverging) flows at high Reynolds numbers.

---

† Present address: Intevep SA, Los Teques (EPPR-32) Apdo. 76343, Caracas 1070-A, Venezuela.

1. Introduction

Though the problem of the determination of the forces exerted by an axisymmetric flow on a sphere has been extensively studied in the literature, there still exist many open questions concerning the effect of the acceleration of either the fluid or the body. More precisely, well-known theoretical results were established early on in the Stokes flow limit (Boussinesq 1885; Basset 1888) as well as in the case of inviscid fluid (see Lamb 1932). Between these two extreme situations the theory is missing and the experimental results are very scarce, whereas most of the numerical investigations have only been concerned with steady uniform flows. The purpose of the study reported here is to fill a part of this gap by investigating numerically various accelerated flows around a sphere at Reynolds numbers in the range $0.1 \leqslant Re \leqslant 300$ ($Re = \rho|V_{rel}|D/\mu$, where D is the sphere diameter, V_{rel} the upstream relative velocity and ρ and μ the density and viscosity of the fluid respectively). Both spatial and temporal accelerations are considered. The present paper (Part 1) only considers steady uniform or non-uniform flows. A companion paper (Part 2, Magnaudet *et al.* 1995) is devoted to uniform unsteady flows. Furthermore, in order for the results to be applicable to both particulate flow and bubbly flow, the cases of a rigid body and a spherical bubble are considered altogether.

The first theoretical studies concerning the forces experienced by a sphere accelerating in an inviscid fluid at rest must be attributed to Poisson and Green as mentioned by Lamb (1932). The result, familiar to students in fluid mechanics, expresses the added mass force $\boldsymbol{F}_M$ versus the acceleration of the sphere $\boldsymbol{a}_P = \mathrm{d}\boldsymbol{V}_P/\mathrm{d}t$, as $\boldsymbol{F}_M = -C_M \rho \mathscr{V} \boldsymbol{a}_P$ ($\boldsymbol{V}_P$ denoting the velocity of the sphere). In this equation $\mathscr{V} = \pi D^3/6$ is the volume of the sphere and C_M is the added mass coefficient equal to $\frac{1}{2}$. If the velocities of both the sphere and the fluid vary in time, an extra term appears representing the part of buoyancy caused by the driving pressure gradient (see for example Batchelor 1967). The total inertia force $\boldsymbol{F}_I$ thus becomes $\boldsymbol{F}_I = \rho \mathscr{V}[\partial \boldsymbol{V}/\partial t + C_M(\partial \boldsymbol{V}/\partial t - \boldsymbol{a}_P)]$, where $\boldsymbol{V}$ denotes the unperturbed fluid velocity. The generalization of this expression to non-uniform fluid motions has been a subject of interest for a long time. Taylor (1928) and Tollmien (1938) carried out pioneering work on this: they calculated the rate of change of the kinetic energy of the inviscid flow around a sphere and found that the body experiences an inertia force. Voinov, Voinov & Petrov (1973); Lhuillier (1982) and Auton, Hunt & Prud'homme (1988) rediscovered and extended these works. All these authors demonstrated that in the expression for $\boldsymbol{F}_I$ the time derivative $\partial \boldsymbol{V}/\partial t$ has to be replaced by the fluid acceleration evaluated at the centre of the sphere, i.e. $\mathrm{D}\boldsymbol{V}/\mathrm{D}t = \partial \boldsymbol{V}/\partial t + \boldsymbol{V} \cdot \boldsymbol{\nabla} \boldsymbol{V}$. This yields

$$\boldsymbol{F}_I = \rho \mathscr{V}[\mathrm{D}\boldsymbol{V}/\mathrm{D}t + C_M(\mathrm{D}\boldsymbol{V}/\mathrm{D}t - \boldsymbol{a}_P)], \tag{1}$$

with the aforementioned value of the added mass coefficient $C_M = \frac{1}{2}$. Very few experiments have been carried out to confirm (1) and to determine C_M in steady non-uniform flows. Taylor (see Auton *et al.* 1988) performed wind tunnel experiments in converging and diverging flows and concluded that the inviscid theory accurately predicts the equilibrium positions of bodies of different forms. Naciri (1992) (see also Bataille, Lance & Marié 1990) determined precisely the equilibrium position of a bubble introduced into a purely rotating flow. From this measurement the author evaluated the rotational lift coefficient $C_{L\Omega}$ related to the lift and added mass coefficients C_L and C_M through $C_{L\Omega} = C_L - \frac{1}{2}(1 + C_M)$. His results agree qualitatively with the inviscid theory of Auton *et al.* (1988) but do not allow a separate determination of C_L and C_M. However, in a separate experiment the same author

evaluated C_M indirectly. Starting from the theoretical result of Darwin (1953) who demonstrated that when a sphere describes a rectilinear motion in an inviscid fluid at rest at infinity the mass displaced by the sphere is equal to the added mass, Naciri measured by optical means the volume of fluid displaced by a bubble in a quiescent liquid and showed that the resulting value of C_M is nearly equal to $\frac{1}{2}$, for Reynolds numbers of the bubble ranging between 500 and 1000. Experimental investigations concerning the added mass force in unsteady flows will be discussed in Part 2.

Concerning viscous flows, nearly all the work reported in the literature up to 1955 was devoted to the effects of temporal acceleration in uniform flows. For example, extending the results of Boussinesq (1885) and Basset (1888), Tchen (1947) showed that when the velocities of both the sphere and the fluid vary in time, the unsteady creeping motion of a rigid sphere of density ρ_P is governed by

$$\boldsymbol{F} = (\rho_P - \rho)\mathscr{V}\boldsymbol{g} + 3\pi\mu D(\boldsymbol{V} - \boldsymbol{V}_P) + \rho\mathscr{V}\left[\frac{\partial \boldsymbol{V}}{\partial t} + C_M\left(\frac{\partial \boldsymbol{V}}{\partial t} - \boldsymbol{a}_P\right)\right] + \tfrac{3}{2}D^2(\pi\mu\rho)^{1/2}\int_{t_0}^{t}\frac{\partial \boldsymbol{V}/\partial\tau - \boldsymbol{a}_P(\tau)}{(t-\tau)^{1/2}}\,\mathrm{d}\tau. \quad (2)$$

The extension of (2) to non-uniform unsteady flow has been the subject of several subsequent papers, containing some errors as discussed by Maxey & Riley (1983). These authors as well as Gatignol (1983) took into account the secondary influence of flow inhomogeneity on the three last terms of (2) and evaluated the corresponding corrections (so-called Faxén forces). Furthermore Maxey & Riley (1983) addressed the question of the generalization of the time derivatives $\partial \boldsymbol{V}/\partial t$ to non-uniform flows. They showed that the first derivative $\partial \boldsymbol{V}/\partial t$ appearing in the right-hand side of (2) must be replaced by the fluid acceleration $\mathrm{D}\boldsymbol{V}/\mathrm{D}t$. In contrast they concluded that in the two last terms of (2), $\partial \boldsymbol{V}/\partial t$ must be replaced by the derivative of $\boldsymbol{V}$ following the moving sphere, i.e. $\mathrm{d}\boldsymbol{V}/\mathrm{d}t = \partial \boldsymbol{V}/\partial t + \boldsymbol{V}_P \cdot \boldsymbol{\nabla}\boldsymbol{V}$. They noted that the corresponding expression for the added mass force differs from that given by (1) and showed that the choice between $\mathrm{D}\boldsymbol{V}/\mathrm{D}t$ and $\mathrm{d}\boldsymbol{V}/\mathrm{d}t$ cannot be made starting from (2) because both expressions become indistinguishable when $Re \ll 1$.

These latter points are underlined to emphasize the fact that difficulties remain in the elaboration of a rational equation of motion for spherical particles. However, such an equation valid at finite Reynolds numbers is highly desirable: it is the key that allows an accurate computation of the trajectories of rigid particles and bubbles in real flows as well as a correct evaluation of momentum exchanges between the particles and the surrounding fluid in dispersed two-phase flows. In particular, several studies have recently appeared where particle dispersion in turbulent flows is studied numerically once the turbulent field has been obtained by direct numerical simulation of the Navier–Stokes equations. It is clear that such an approach is very powerful but that a reliable description of the turbulent flow is not sufficient: results are general and accurate only if the dynamic equation governing the motion of the particles is able to take into account the influence of flow inhomogeneity and unsteadiness on the instantaneous drag. A way to contribute to these questions is to begin by computing and examining carefully several very simple accelerated flows where only one or two effects are present in each. This first step provides a unique way to determine clearly the evolution of several coefficients involved in the expression for the hydrodynamic forces as well as the correct form of these forces. When such studies are available for quite different situations a first approximation of the general expression for the

hydrodynamic forces could be obtained by superposition. In a final step this expression could be refined by studying more complicated situations involving coupled effects.

The present work belongs clearly to the first step of this general approach. Using the same guideline Part 2 is devoted to uniform unsteady flows at finite Reynolds number. In the present paper we only present results obtained in steady flows. Uniform flow is examined first as a reference. Then the simplest steady non-uniform flow with spatial acceleration, namely purely straining flow, is studied. At first glance this flow looks quite academic with respect to real situations because a particle moving in a straining flow experiences not only a spatial acceleration but also transient effects. However, in the spirit of the foregoing discussion we believe that this flow contains some essential features which allow to address the following questions:

(i) can the result expressed by (1) for inviscid non-uniform flow be extended to viscous flow and if so, how does the added mass coefficient depend on the Reynolds number?

(ii) are there specific viscous effects induced by steady accelerated flows?

(iii) what is the proper generalization to non-uniform flows of the fluid acceleration involved in the history force of (2)?

(iv) does the flow around a rigid sphere exhibit a different behaviour from that around a spherical bubble?

2. Numerical method

2.1. *Governing equations*

The problem of determining the hydrodynamic forces on a sphere in accelerated flows requires the solution of the unsteady axisymmetrical Navier–Stokes equations. Unlike most of the earlier works devoted to the steady flow around a sphere (where the Navier–Stokes equations were solved using the stream-function/vorticity formulation), the formulation using the primitive velocity–pressure variables is adopted in the present study. Furthermore the equations are written in general orthogonal coordinates instead of the usual spherical coordinates. These computational choices give a lot of flexibility and allow the present code to be used for solving quite complicated problems.

To write the resolved equations let us introduce the contravariant velocity component V_i along the coordinate line ξ_i' and the physical length $\mathrm{d}\xi_i = h_i \mathrm{d}\xi_i$ (h_i denoting the metric factor along the direction ξ_i' and no summation being assumed on i). Defining the stretching factors

$$H_i^j = h_i^{-1} \partial h_i / \partial \xi_j \tag{3}$$

and the generalized divergence operator

$$\boldsymbol{\nabla} \cdot_{(i)} ( ) = \partial ( ) / \partial \xi_i + \sum_{k \neq i} H_i^k ( ), \tag{4}$$

the equations can be written in the compact conservative form (Pope 1978):

$$\sum_j \boldsymbol{\nabla} \cdot_{(j)} V_j = 0, \tag{5}$$

$$\frac{\partial V_i}{\partial t} + \sum_j \boldsymbol{\nabla} \cdot_{(j)} (V_i V_j - \tau_{ij}) = -\frac{1}{\rho} \frac{\partial P}{\partial \xi_i} - \sum_j H_i^j (V_j V_i - \tau_{ji}) + \sum_j H_j^i (V_j V_j - \tau_{jj}), \tag{6}$$

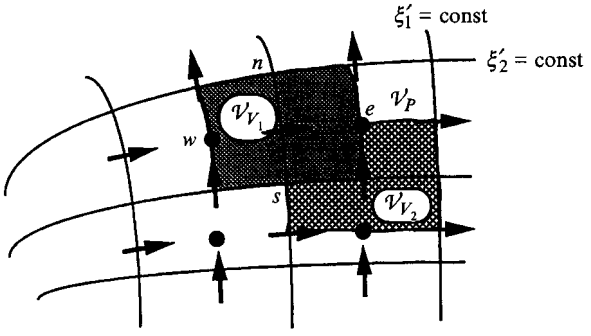

FIGURE 1. Typical staggered finite-volume cells: ●, pressure node; →, V_1 node; ↑, V_2 node.

where P denotes the pressure, ρ the density and τ_{ij} the components of the viscous stress tensor given by

$$\tau_{ij} = \nu\left\{\frac{\partial V_i}{\partial \xi_j}+\frac{\partial V_j}{\partial \xi_i}-H_j^i V_j-H_i^j V_i+2\sum_k H_i^k V_k \delta_{ij}\right\}, \tag{7}$$

ν being the kinematic viscosity. Equations (5) and (6) can also be written in the integral form

$$\sum_j \int_{\mathscr{A}} V_j n_j \,\mathrm{d}\mathscr{A} = 0, \tag{8}$$

$$\int_{\mathscr{V}} \frac{\partial V_i}{\partial t}\mathrm{d}\mathscr{V} = -\int_{\mathscr{V}} \frac{1}{\rho}\frac{\partial P}{\partial \xi_i}\mathrm{d}\mathscr{V} + \sum_j \int_{\mathscr{V}} [H_j^i(V_j V_j-\tau_{jj})-H_i^j(V_j V_i-\tau_{ji})]\,\mathrm{d}\mathscr{V}$$
$$+\sum_j \int_{\mathscr{A}} (\tau_{ij}-V_i V_j) n_j \,\mathrm{d}\mathscr{A}. \tag{9}$$

2.2. *Spatial approximations and grid system*

We use a finite-volume approach in which both components of (6) are first written at the velocity nodes of a staggered mesh (see Harlow & Welch 1965) then integrated in the form (9) on the corresponding volumes shown in figure 1. Let us consider for example the V_1 equation (V_1 and V_2 denoting the velocity components along the coordinates lines $\xi_2' = \text{const.}$ and $\xi_1' = \text{const.}$ respectively). In a way consistent with second-order accuracy we assume the source terms to be constant on the volume $\mathscr{V}_{V_1}$ and each flux term to be constant on the corresponding surface $\mathscr{A}$ so that the V_1 equation can be written, following the notation of figure 1,

$$\left(\frac{\partial V_1}{\partial t}\right)_{V_1} \mathscr{V}_{V_1} + (V_1\langle V_1 \mathscr{A}\rangle - \tau_{11}\mathscr{A})_e - (V_1\langle V_1 \mathscr{A}\rangle - \tau_{11}\mathscr{A})_w$$
$$+(V_1\langle V_2 \mathscr{A}\rangle - \tau_{12}\mathscr{A})_n - (V_1\langle V_2 \mathscr{A}\rangle - \tau_{12}\mathscr{A})_s$$
$$= -\left(\frac{\partial P/\rho}{\partial \xi_1}\right)_{V_1} \mathscr{V}_{V_1} + [H_2^1(V_2 V_2-\tau_{22})-H_3^1\tau_{33}-H_1^2(V_2 V_1-\tau_{12})]_{V_1}\mathscr{V}_{V_1}. \tag{10}$$

All the spatial derivatives are approximated using second-order central differences evaluated directly in the physical domain. Owing to the relative position of V_1, V_2 and P nodes (to be described later), second-order accuracy requires only two-point differences except for the evaluation of the normal derivatives $\partial V_1/\partial \xi_1$ and $\partial V_2/\partial \xi_2$ involved in the viscous stresses. These two terms require a three-point formula on non-uniform meshes and they are actually evaluated using four points so as to preserve

spatial symmetry. Equation (10) contains advective fluxes whose evaluation requires velocity components to be known at P nodes and at vertices of $\mathscr{V}_P$. In a similar way the curvilinear terms of the right-hand side require viscous stresses and velocities V_2 to be evaluated at the nodes of V_1. This is achieved through a linear interpolation procedure which guarantees second-order accuracy. A different procedure is used to evaluate the mass fluxes involved from advective terms (the angle-bracketed terms of the left-hand side): since a mass balance is only specified on $\mathscr{V}_P$ cells it is easy to show that in curvilinear meshes mass is not *a priori* conserved on $\mathscr{V}_{V_1}$ and $\mathscr{V}_{V_2}$. To guarantee this conservation, bracketed mass fluxes are calculated as a whole through a linear interpolation of mass fluxes crossing the corresponding boundaries of the two contiguous $\mathscr{V}_P$ cells (Galpin & Raithby 1986).

Let us now describe briefly the main characteristics associated with the generation of the curvilinear mesh. A rectangular mesh is first defined in the numerical plane (ξ_1', ξ_2'). Grid control is performed at this stage so that the (ξ_1', ξ_2') mesh is non-uniform. V_1 and V_2 nodes are located midway between two neighbouring pressure nodes in this plane. This arrangement allows one to compute second-order-accurate first derivatives with a two-point formula on Cartesian or polar grids. Then the locations of the P nodes and the locations of the vertices of $\mathscr{V}_{V_1}$, $\mathscr{V}_{V_2}$ and $\mathscr{V}_P$ are mapped on the physical domain through a numerical or an analytical mapping. For a single sphere or a circular cylinder of radius R embedded in an infinite domain, a conformal mapping can be obtained very easily since the equations defining the streamlines $\Psi = \text{const.}$ and the equipotential lines $\phi = \text{const.}$ are known analytically (Conner & Elgobashi 1987). Equations corresponding to the potential flow around a cylinder have been selected because they are easier to handle numerically. Defining a polar coordinate system (θ, r) centred on the sphere (the angle θ increasing clockwise with $\theta = 0$ along the negative part of the ξ_1' axis), a point M' of the numerical plane $(\xi_1' = \phi, \xi_2' = \Psi)$ is associated with a point M of the physical plane (θ, r) through the transformation

$$\phi = -\cos\theta(r + R^2/r), \tag{11}$$

$$\Psi = \sin\theta(1 - R^2/r^2). \tag{12}$$

It is worth noting that after the mapping the relative positions of velocity and pressure nodes within a cell are slightly modified by the stretching factors H_1^1 and H_2^2. However, it is straightfoward to show that these modifications only occur at second order. This is the reason why two-point differences remain second-order accurate on the curvilinear mesh except perhaps in the vicinity of singular points of the mapping.

Near the sphere the curvilinear terms of (9) have an important weight and it is crucial to evaluate correctly the radii of curvature H_1^2, H_2^1, H_3^2 and H_1^3 (H_1^3 and H_2^3 are zero since the system is axisymmetrical). This is achieved easily with the aid of an integral formulation: it is straightforward to show for example that

$$(H_1^2)_U \mathscr{A}_{V_1} = \mathscr{L}_n - \mathscr{L}_s, \tag{13}$$

where $\mathscr{A}_{V_1}$ denotes the surface of the V_1 cell in the (x, y) plane, whereas $\mathscr{L}_n$ and $\mathscr{L}_s$ are the lengths of the arcs bounding $\mathscr{A}_{V_1}$ and belonging to $\mathscr{A}_n$ and $\mathscr{A}_s$ respectively. A similar expression can be obtained for the other radii of curvature. This procedure has been found to produce far better estimations than a direct numerical evaluation of the geometrical definition of the H_i^j.

2.3. *Time advancement of the solution*

The solution is advanced in time through the following algorithm: the fractional-step method proposed by Braîlovskaya (1965) is employed to stabilize the advective terms discretized with the centred scheme previously described, whereas incompressibility is

satisfied by using the SMAC method of Amsden & Harlow (1972). Depending on the flow Reynolds number, viscous terms are evaluated explicitly or implicitly so as to remove the stability constraint imposed by diffusion. Let us describe the complete algorithm in the simplest case of an explicit evaluation of the viscous terms. Using for compactness the local form of the momentum equation (6) and denoting by SA_i and SV_i the advective and viscous parts of the curvilinear source terms respectively, the algorithm is as follows.

Predictor step

$$\frac{V_i^* - V_i^n}{\Delta t} + \sum_j \nabla\cdot_{(j)}(V_i^n V_j^n - \tau_{ij}^n) = -\frac{1}{\rho}\frac{\partial P^n}{\partial \xi_i} + SA_i^n + SV_i^n, \tag{14a}$$

$$\tilde{V}_i^{n+1} - V_i^* = -\frac{\Delta t}{\rho}\frac{\partial \tilde{\Phi}^{n+1}}{\partial \xi_i}. \tag{14b}$$

Since the predictor velocity $\tilde{V}_i^{n+1}$ must be divergence-free the auxiliary pressure $\tilde{\Phi}^{n+1}$ satisfies the Poisson equation

$$\nabla^2 \tilde{\Phi}^{n+1} = \frac{\rho}{\Delta t}\sum_j \nabla\cdot_{(j)} V_j^*. \tag{15}$$

Corrector step

$$\frac{\tilde{V}_i^* - \tilde{V}_i^{n+1}}{\Delta t} + \sum_j \nabla\cdot_{(j)}(\tilde{V}_i^{n+1}\tilde{V}_j^{n+1} - V_i^n V_j^n) = \widetilde{SA}_i^{n+1} - SA_i^n, \tag{16a}$$

$$V_i^{n+1} = \tilde{V}_i^* - \frac{\Delta t}{\rho}\frac{\partial \Phi^{n+1}}{\partial \xi_i}, \tag{16b}$$

with Φ^{n+1} satisfying

$$\nabla^2 \Phi^{n+1} = \frac{\rho}{\Delta t}\sum_j \nabla\cdot_{(j)} \tilde{V}_j^*. \tag{17}$$

The pressure field at time $(n+1)\Delta t$ is then given by

$$P^{n+1} = P^n + \Phi^{n+1}. \tag{18}$$

This algorithm provides a solution which is first-order accurate in time. Since the matrix resulting from the Poisson equation need only be inverted once at the beginning of the computation, this explicit algorithm which is made stable for CFL numbers less than unity is very efficient.

2.4. *Boundary conditions*

Two types of boundary conditions deserve a few comments since they are not provided directly by the physics. The first type is the set of conditions needed to treat the boundaries where the flow leaves the computational domain. No physically meaningful condition exists for such boundaries and the development of absorbing conditions avoiding perturbations of the flow is still an active area in computational fluid dynamics. The heuristic technique used in the present study is as follows. Evaluation of advection, diffusion and normal pressure gradient in the momentum equations (9) written in cells adjacent to an outflow boundary requires *a priori* knowledge of velocity components and pressure downstream. For this purpose a row of fictitious cells is introduced downstream from the boundary. In such cells, the tangential and normal velocity components V_T and V_N (defined with respect to the boundary under consideration) and the pressure P are evaluated explicitly using the information

available upstream and assuming that right at the boundary the flow field satisfies the set of parabolic approximations

$$\frac{\partial^2 V_N}{\partial N^2} = 0, \quad \frac{\partial V_T}{\partial N} = 0, \quad \frac{\partial^2 P}{\partial T \partial N} = 0 \tag{19a–c}$$

($\partial/\partial N$ and $\partial/\partial T$ denote the normal and tangential derivatives respectively). Condition (19c) traduces the momentum balance of $\partial V_T/\partial N$ obtained within the parabolic approximation. The normal derivatives of $\tilde{\Phi}^{n+1}$ and Φ^{n+1} are also needed to obtain the normal velocity right on the boundary (see (14b)–(16b) and figure 1). Since (18) does not hold in the ficticious cells, the condition on the auxiliary pressure is not dictated by condition (19c) in such cells. Thus it is assumed that during a time step the pressure remains frozen in the fictitious cells, i.e.

$$\tilde{\Phi}^{n+1} = \Phi^{n+1} = 0. \tag{20}$$

Using condition (20) and the values of V_T, V_N, P determined by conditions (19a–c), the momentum equations (9) are solved in the last row of cells located upstream from the boundary as for a standard cell.

A second set of boundary conditions which is not straightforwardly provided by the physics is needed on boundaries where the normal velocity V_N is given (but can vary in time): because of the use of a fractional-step method it is necessary to prescribe conditions for the intermediate fields V_N^* and $\tilde{V}_N^*$. When viscous terms are treated explicitly the condition can be chosen arbitrarily (Peyret & Taylor 1983). When an implicit scheme is used it can be shown, following the analysis of Moin & Kim (1985), that with the present algorithm the correct boundary condition for these quantities is

$$V_N^* = \tilde{V}_N^{n+1} = \tilde{V}_N^* = V_N^{n+1}. \tag{21}$$

Consequently the condition (21) is used on such boundaries whatever the scheme employed for viscous terms. As is well known no condition on the pressure P is needed at the boundary. However, in a way consistent with (14b) and (16b) the auxiliary pressures $\tilde{\Phi}^{n+1}$ and Φ^{n+1} obey

$$\frac{\partial \tilde{\Phi}^{n+1}}{\partial N} = \frac{\partial \Phi^{n+1}}{\partial N} = 0. \tag{22}$$

2.5. *Preliminary testing*

Before being used to compute flows around a sphere, the code was extensively tested. Details of the tests can be found in Rivero (1991). The spatial and temporal accuracy was determined by simulating the Green–Taylor vortex for which an analytical solution of the full time-dependent Navier–Stokes equation exists. The results confirmed that spatial accuracy is of second order while temporal accuracy is of first order. The driven-cavity problem with a parabolic slip velocity was treated to evaluate the effects of numerical diffusion. Results were compared to those reported by Peyret & Taylor (1983). The solution given by the present code was found to lie closer to the reference solution (obtained with a fourth-order Hermitian method) than all other second-order-accurate solutions reported in the comparison. The influence of the outlet conditions (19a–c) and (20) was first evaluated by computing the development of a Poiseuille flow in a circular pipe. Results showed that the parabolic velocity profile found in the outlet plane was exactly identical to those obtained in the preceding cross-sections. More severe tests were performed later including situations where vortices or internal waves (generated by coupling (8) and (9) with a density equation) leave the domain. Conditions (19a–c) and (20) were found to work well in all cases.

A second series of tests was carried out in order to determine the optimal

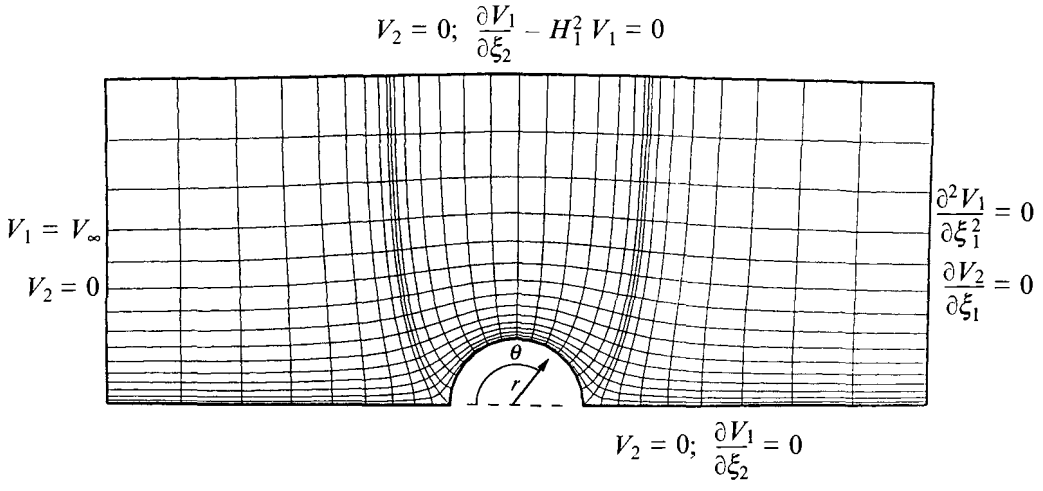

FIGURE 2. Partial view of the (ϕ, Ψ) mesh with outer boundary conditions.

characteristics of the mesh to be used for computing the flow around a bluff body. For this purpose two well-documented steady flows, namely the flow around a circular cylinder at $Re = 20$ and that around a rigid sphere at $Re = 100$ were studied. Results obtained using polar (or spherical) coordinates were compared to those obtained with the (ϕ, Ψ) coordinate system defined by (11) and (12). Potential flow conditions were used on the outer circular boundary in the first case. With the second grid the inflow, free-stream and outflow boundary conditions shown in figure 2 were imposed on the velocity field together with conditions (22), and (19*c*) and (20) for the pressure as discussed in the previous subsection. Results obtained for the circular cylinder using the polar grid showed that quantities such as separation angle and reattachment length of the separated region were sensitive to the outer radius R_∞ even for ratios R_∞/R as large as 130. In contrast satisfactory results were obtained with the (ϕ, Ψ) grid using much smaller values of ϕ_∞ and Ψ_∞. For that reason the (ϕ, Ψ) grid and the aforementioned set of outer conditions are used in all the simulations reported in this work. To determine the optimal size of the computational domain the flow at $Re = 100$ around a rigid sphere was computed using several values of ϕ_∞ and Ψ_∞. A value of 40 produced satisfactory results but the value of 80 was finally retained for all the computations in order to avoid confinement effects in low-Re flows. Thus the computational domain shown in figure 2 actually extends up to 80 radii of the sphere upstream and downstream as well as along the direction normal to the symmetry axis. An exponential distribution of grid points centred on the sphere was chosen along both directions. The number of grid points was determined so that the solution was grid-independent. This led to a 72×36 grid with only 15 points on the sphere: comparisons made with simulations using up to 32 points on the sphere did not show any significant difference between both solutions. A comparison of results obtained with the 72×36 (ϕ, Ψ) grid and with a 32×32 spherical grid is shown in figure 3(*a*, *b*): vorticity and pressure distributions found at the surface of the sphere with both grid systems are very close, even near the stagnation point where curvatures of the (ϕ, Ψ) grid are very severe. Furthermore both results compare very well with those found by Le Clair, Hamielec & Pruppacher (1970).

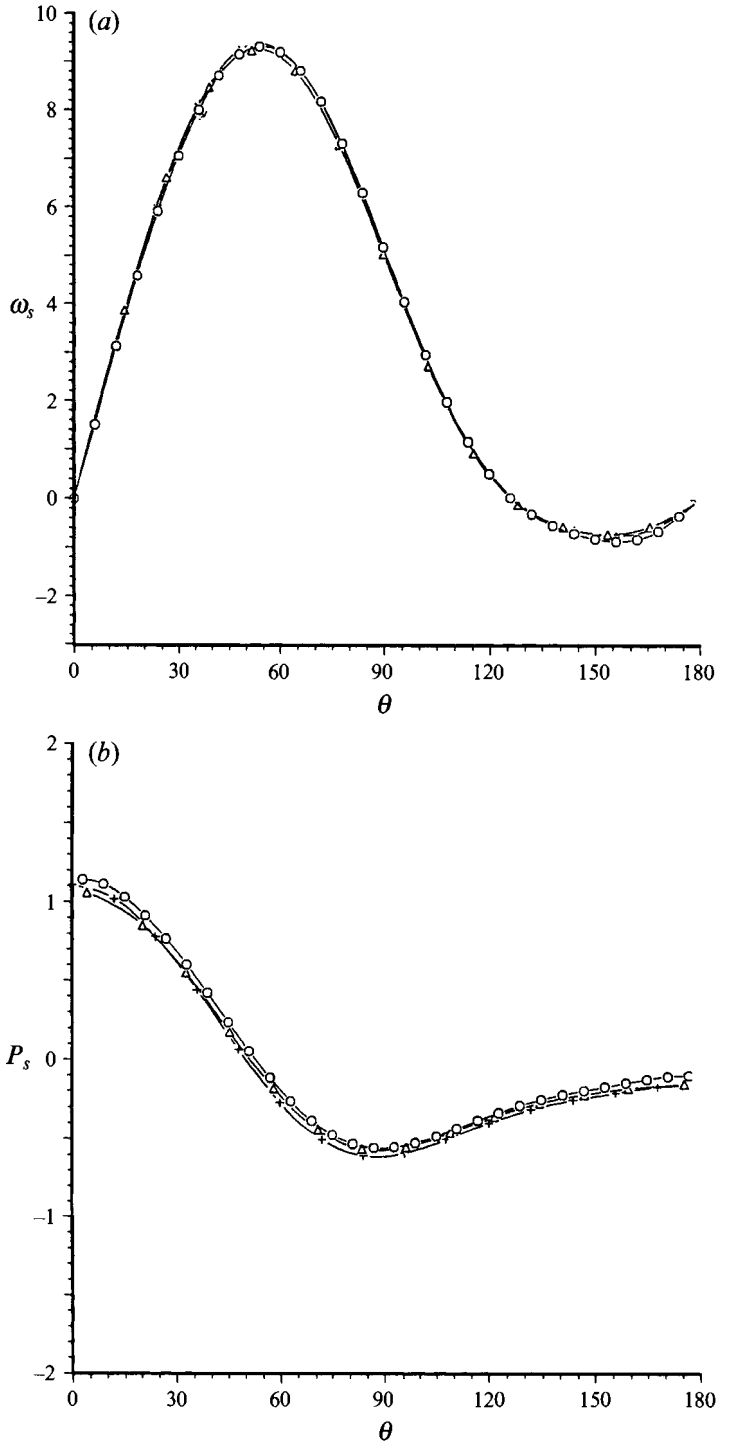

FIGURE 3. Comparison of surface distributions obtained with a spherical grid and with the (ϕ, Ψ) grid (rigid sphere at $Re = 100$). (In all figures vorticities and pressures are normalized by $2V_0/D$ and $\frac{1}{2}\rho V_0^2$ respectively.) (*a*) Vorticity; (*b*) pressure: ○, spherical grid; △, (ϕ, Ψ) grid, +, LeClair *et al.* (1970).

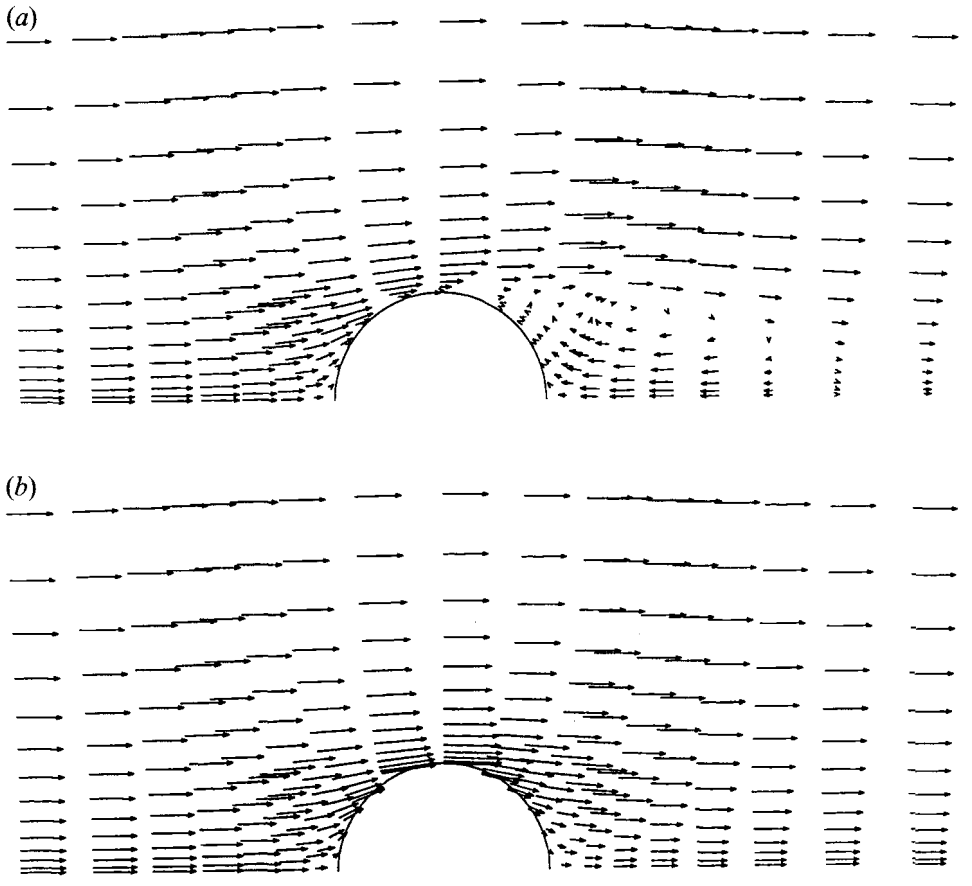

FIGURE 4. Velocity field around a sphere in a uniform steady flow ($Re = 300$): (*a*) rigid sphere, (*b*) inviscid bubble.

3. Steady uniform flow

3.1. *General considerations*

Before dealing with accelerated flows we start by considering uniform steady flows around a rigid sphere or a spherical bubble. This situation has already been studied numerically by many authors, in particular Rimon & Cheng 1969; Le Clair *et al.* 1970; Dennis & Walker 1971; Fornberg 1988 for the rigid sphere; and Brabston & Keller 1975; Ryvkind & Ryskin 1976; Oliver & Chung 1987 for the inviscid bubble. However, this step is necessary in order to perform comparisons with accelerated situations and more precisely in order to determine in such cases the net effect of acceleration evaluated with the same computational tool.

The present work only considers Reynolds number up to 300 because this limit corresponds roughly to the transition region between axisymmetric flow and non-axisymmetric vortex shedding regime for rigid spheres (Achenbach 1974) and to the appearance of the first significant deviations from sphericity for air bubbles in water. However, it must be noted that in the case of the rigid sphere, considerable uncertainty exists concerning the critical Reynolds number Re_c at which non-axisymmetric flow appears: most experiments do not detect vortex shedding before $Re = 400$ (Clift, Grace & Weber 1978) but Sakamoto & Haniu (1990) reported a value of Re_c roughly equal to 300. Up to now numerical stability analyses of the flow behind a sphere are not in

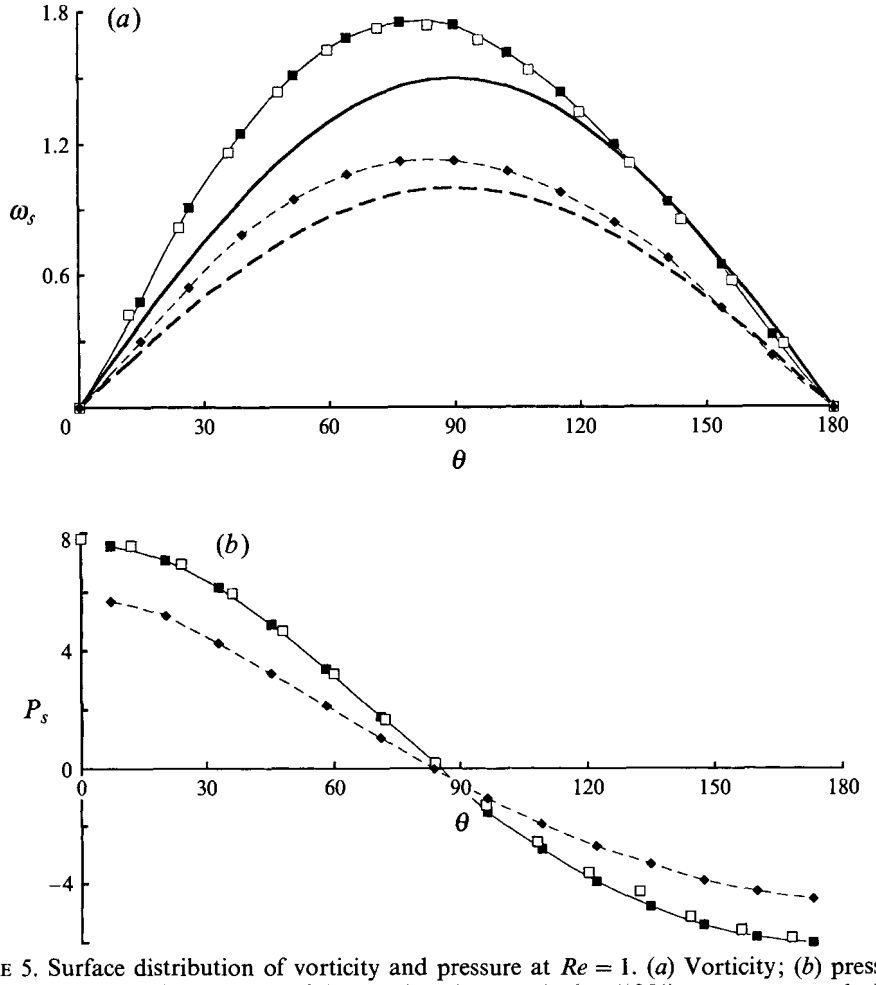

FIGURE 5. Surface distribution of vorticity and pressure at $Re = 1$. (*a*) Vorticity; (*b*) pressure: ■, present study (rigid sphere); □, LeClair *et al.* (1970); ——, Stokes (1851); ◆, present study (bubble); – – –, Hadamard–Rybczynski (1911).

agreement either on the value of Re_c or on the nature of the transition to non-axisymmetric flow: Kim & Pearlstein (1990) found a Hopf bifurcation at $Re_c = 175.1$ while Natarajan & Acrivos (1993) found a regular bifurcation at $Re_c = 210$. These uncertainties suggest that the results presented hereafter for the steady flow at $Re = 300$ must be taken with caution.

The flows are computed using the grid and the outer boundary conditions already described. On the body no-slip conditions are imposed for the rigid sphere, i.e.

$$V_1 = 0, \quad V_2 = 0, \tag{23a, b}$$

whereas the bubble surface is considered as a shear-free interface, i.e.

$$\partial V_1/\partial \xi_2 - H_1^2 V_1 = 0 \quad (H_1^2 = 1/R \text{ on the sphere}), \quad V_2 = 0. \tag{24a, b}$$

3.2. *Local distributions: velocity and surface parameters*

The qualitative difference between the flow around a rigid sphere and that around an inviscid bubble is particularly prominent at high Reynolds numbers. It is clearly illustrated by comparing the velocity fields at $Re = 300$ plotted on figure 4(*a*, *b*): figure 4(*a*) shows the large separated region followed by a very pronounced wake which exists

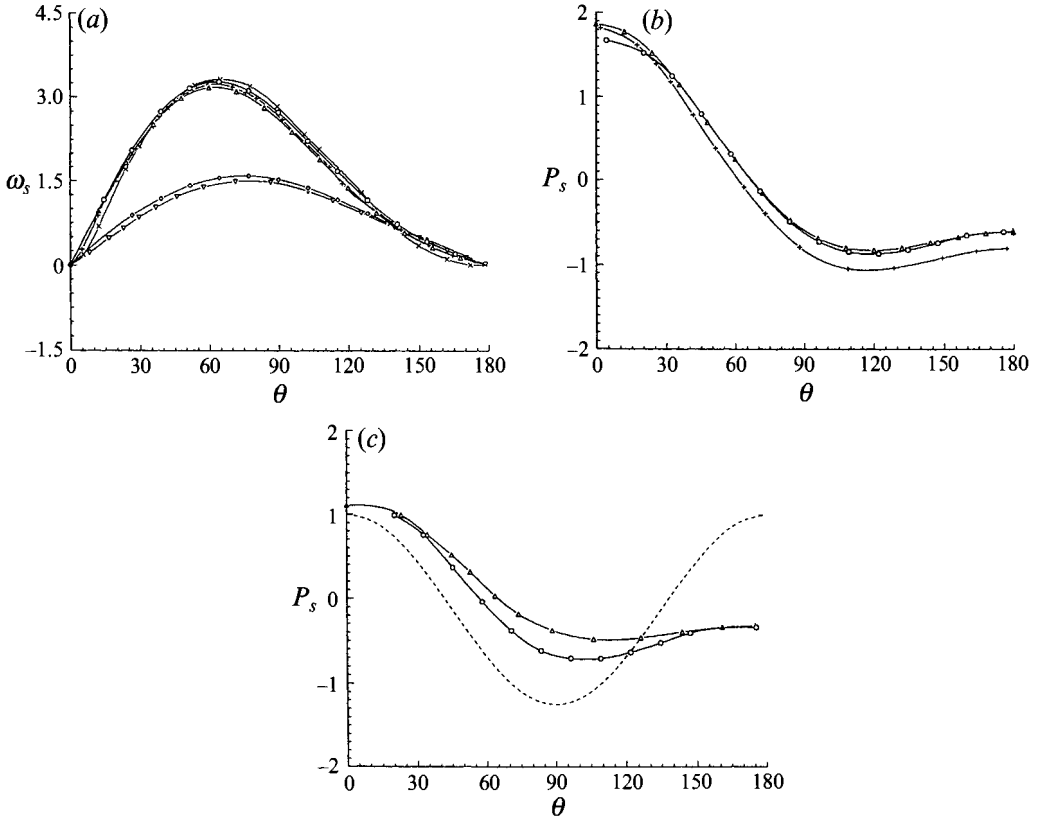

FIGURE 6. Surface distribution of vorticity and pressure at $Re = 10$. (*a*) Vorticity, (*b*) pressure (rigid sphere): ○, present study (rigid sphere); △, LeClair *et al.* (1970); +, Dennis & Walker (1971); ×, Rimon & Cheng (1969); ◇, present study (bubble); ▽, Brabston & Keller (1975). (*c*) Pressure (bubble): ○, present study; △, Brabston & Keller (1975); ----, potential solution.

at the rear of the rigid sphere while figure 4(*b*) shows that only a small asymmetry exists between upstream and downstream regions near the bubble. Furthermore the velocity profile at the top of the sphere shows that the boundary layer around the rigid sphere is thick while for the bubble maximum velocity is located very near the surface.

These differences can be analysed more precisely by examining the distributions of vorticity and pressure at the surface. Let us first define precisely these quantities. Since the flow is assumed axisymmetric the only component of vorticity lies in the azimuthal direction and is given by

$$\omega = \frac{\partial V_1}{\partial \xi_2} + H_1^2 V_1 - \frac{\partial V_2}{\partial \xi_1} - H_2^1 V_2. \tag{25}$$

Owing to boundary conditions (23) and (24), this reduces at the surface to

$$\omega_s = \partial V_1/\partial \xi_2 \text{ for the rigid sphere}, \quad \omega_s = 2H_1^2 V_1 \text{ for the inviscid bubble.} \tag{26a, b}$$

The pressure at the surface is defined as $P_s = (P - P_0)$ where P_0 denotes a pressure reference chosen on the upstream boundary. Since the pressure is not directly known at the surface its value on the sphere is calculated using a two-point second-order-accurate extrapolation. Vorticities and pressures shown in the figures are scaled by $2V_\infty/D$ and $\frac{1}{2}\rho V_\infty^2$ respectively (note that since the sphere is set fixed the relative velocity V_{rel} is equal to the upstream fluid velocity V_∞).

Surface vorticities and pressures are plotted on figures 5–8 for Reynolds numbers 1,

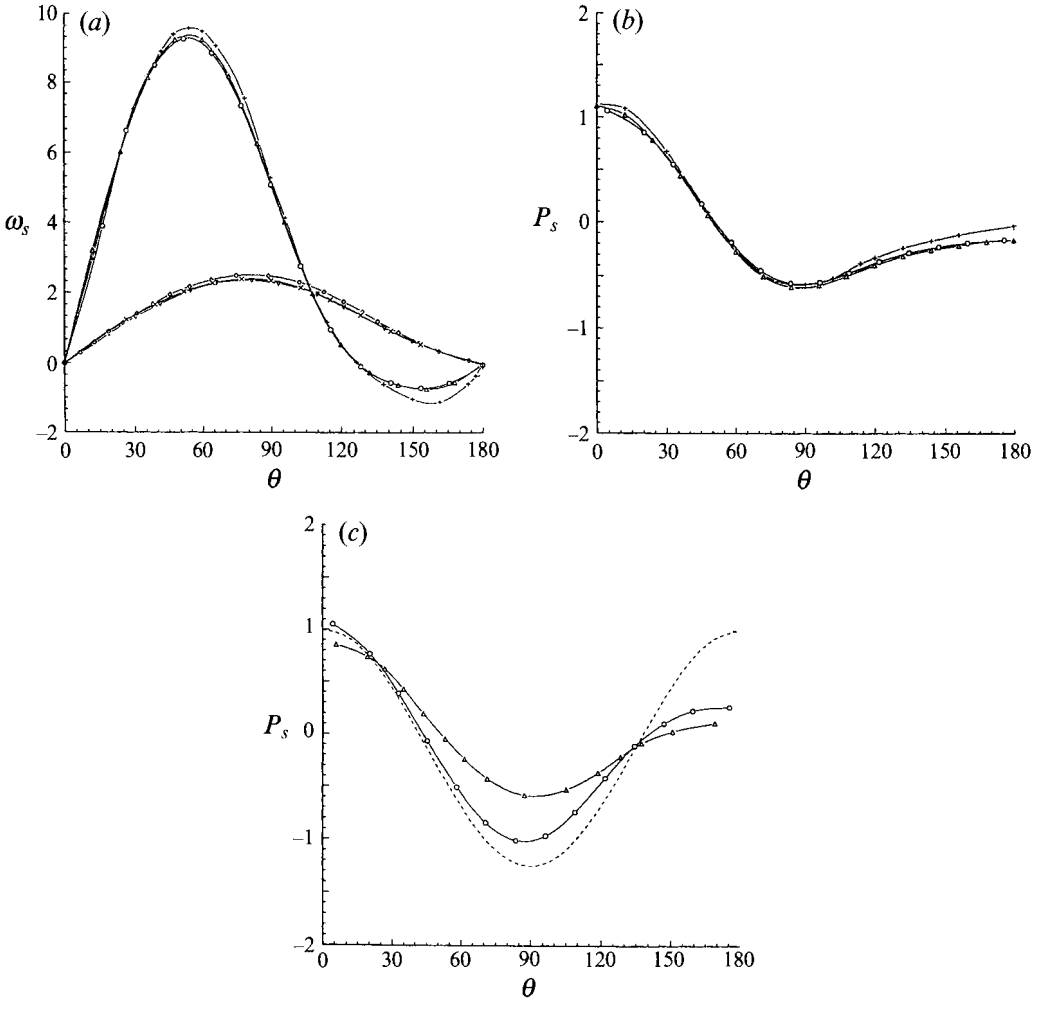

FIGURE 7. Surface distribution of vorticity and pressure at $Re = 100$. (*a*) Vorticity, (*b*) pressure (rigid sphere): ○, present study (rigid sphere); △, LeClair *et al.* (1970); +, Rimon & Cheng (1969); ×, present study (bubble); ◇, Brabston & Keller (1975). (*c*) Pressure (bubble): ○, present study; △, Brabston & Keller (1975); ——, potential solution.

10, 100 and 300 and compared with some available theoretical or numerical results. Distributions of vorticity show striking differences between the rigid sphere and the inviscid bubble: while for the bubble they remain nearly symmetric with respect to $\theta = \frac{1}{2}\pi$ whatever the Reynolds number, they become increasingly asymmetric for the rigid sphere. In this latter case a region of negative values appears for $Re \geqslant 20$. When Re increases from 1 to 300 the maximum vorticity increases by one order of magnitude for the rigid sphere and only by a factor of 3 for the bubble. The evolution with Re of the pressure at the surface of the bubble shows that when Re increases this quantity goes from the odd distribution typical of creeping motion to the even distribution characteristic of potential flow. At $Re = 300$ the pressure differs significantly from the potential solution only in the region located near the rear stagnation point. In contrast a strong asymmetry remains at the surface of the rigid sphere because the pressure tends to stay nearly constant on the half-rear.

Comparisons of these results with those of previous investigators show a very good

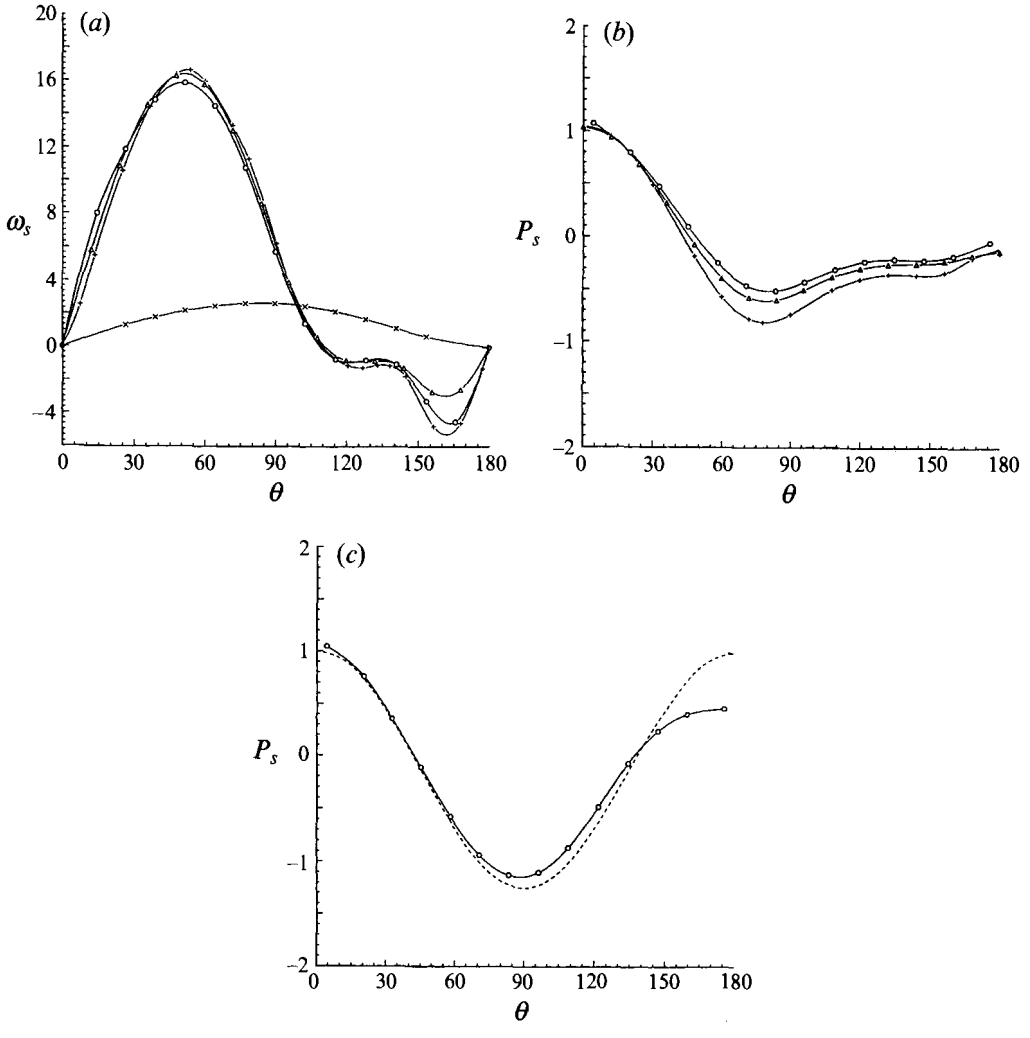

FIGURE 8. Surface distribution of vorticity and pressure at $Re = 300$. (*a*) Vorticity, (*b*) pressure (rigid sphere): ○, present study (rigid sphere); △, LeClair *et al.* (1970); +, Rimon & Cheng (1969); ×, present study (bubble). (*c*) Pressure (bubble): ○, present study; ---, potential solution.

agreement for vorticity distributions, especially those found by Le Clair *et al.* (1970) for the rigid sphere and by Brabston & Keller (1975) for the inviscid bubble. For the pressure at the surface a very good agreement is again found with the results of Le Clair *et al.* (1970). In contrast significant discrepancies, increasing with *Re*, exist near the top of the bubble with the results of Brabston & Keller (1975). This difference is probably due to the method of truncated series used by those authors: their method did not contain enough terms to deal with Reynolds numbers beyond 50 (see Dennis & Walker 1971).

3.3. *Global parameters: characteristics of the separated region and drag coefficient*

For a rigid sphere it is well known (see e.g. Batchelor 1967) that a separated region appears for a critical Reynolds number $Re_c \approx 20$. The critical value found in the present simulations is precisely 20.0. The two main characteristic parameters of this separated region, namely the separation angle and the reattachment length on the

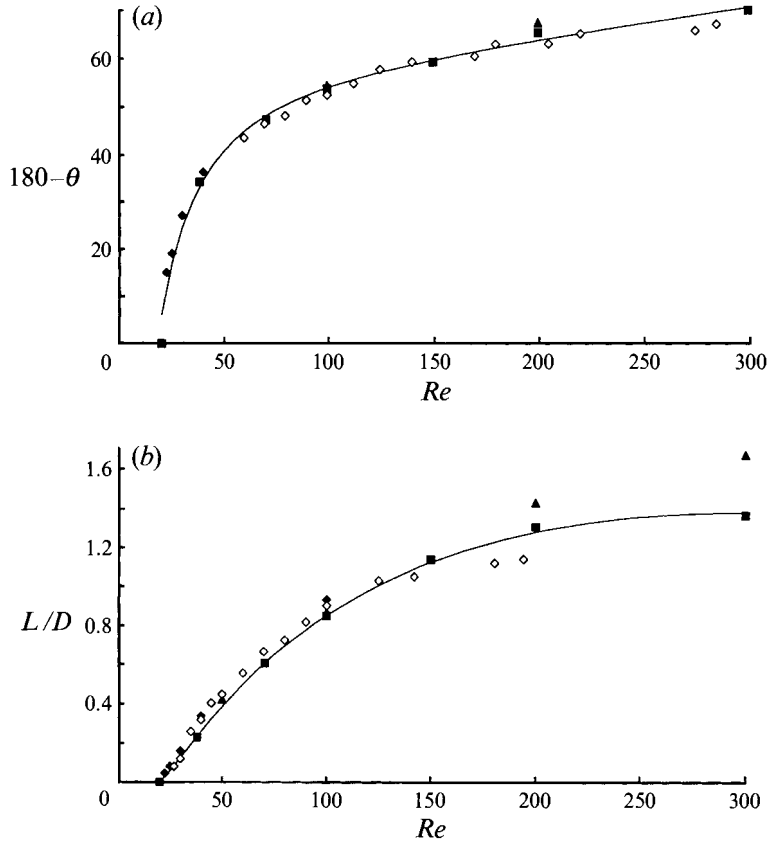

FIGURE 9. Characteristics of the separated region behind a rigid sphere in a uniform steady flow. (*a*) Separation angle (measured from the rear stagnation point), (*b*) reattachment length: ■, present study; ▲, Fornberg (1988); ◆, Pruppacher *et al.* (1970); ◇, Taneda (1956).

symmetry axis, are determined by an interpolation procedure. Their evolution with Re is shown in figure 9(*a*, *b*) and compared to the experimental results of Taneda (1956) and to the numerical predictions of Pruppacher, Le Clair & Hamielec (1970) and Fornberg (1988). A very good agreement is found for the separation angle for all approaches. Concerning the reattachment length, a similar agreement is found for $Re \leqslant 150$ but appreciable differences appear for higher values of Re, especially with the data of Fornberg (1988). This discrepancy has probably the same origin as that observed in figure 8(*a*) ($Re = 300$) with the results of Le Clair *et al.* (1970) in the separated region: these two groups of authors performed strictly steady computations while the present algorithm enables internal unsteadiness to exist in the flow. As a consequence the standing eddy slowly oscillates along the symmetry axis for $Re > 150$. The characteristics of the separated region are undoubtly modified by this oscillation and it can be noted in figure 9(*b*) that our results for the recirculation length behave qualitatively as those obtained experimentally by Taneda (1956) who observed a similar oscillation for $Re > 130$.

The drag force F_D experienced by the sphere is computed by integrating the stress tensor on the surface according to the definition:

$$F_D = \int_S \{\boldsymbol{e}_z \cdot \boldsymbol{n}(-P + \tau_{NN}) + \boldsymbol{e}_z \cdot \boldsymbol{t}\tau_{TN}\}\,\mathrm{d}S, \tag{27}$$

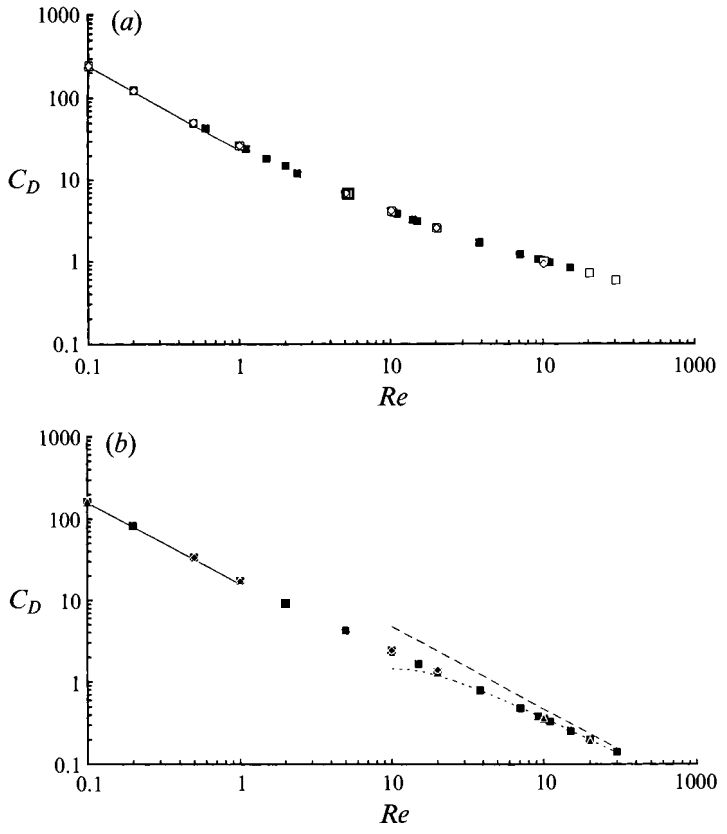

FIGURE 10. The drag coefficient in a uniform steady flow. (*a*) Rigid sphere: ■, present study; □, LeClair *et al.* (1970); ◇, Dennis & Walker (1971); ——, Stokes (1851). (*b*) Inviscid bubble: ■, present study; ▲, Brabston & Keller (1975); ◆, Ryvkind & Ryskin (1976); ——, Hadamard–Rybczynski (1911); – – –, Levich (1949, 1962); · · · ·, Moore (1963).

where τ_{NN} and τ_{TN} denote the normal and tangential viscous stresses respectively while $\boldsymbol{e}_z$, $\boldsymbol{n}$ and $\boldsymbol{t}$ are unit vectors along the streamwise, normal and tangential local directions respectively. In fact only one viscous contribution appears for each kind of sphere since τ_{TN} is zero for the bubble whereas conditions (23*a*, *b*) combined with continuity show that τ_{NN} vanishes at the surface of the rigid sphere. Normal stresses which are only known at pressure nodes are extrapolated on the surface using the same procedure as for pressure. As usual we introduce the drag coefficient C_D defined by

$$F_x = C_D \tfrac{1}{8}\pi D^2 \rho V_\infty^2. \tag{28}$$

According to (27), C_D is split into a pressure drag coefficient C_{PD} and a viscous contribution C_{VD}. Figure 10(*a*, *b*) displays the evolution of C_D with the Reynolds number for the rigid sphere and the bubble respectively. Values of C_{VD} and C_{PD} obtained for ten Reynolds numbers ranging between 0.1 and 300 are reported in tables 1 and 2 and are compared to those found in previous numerical studies and to some well-known asymptotic results. The present values agree well with those found by Le Clair *et al.* (1970) for the rigid sphere and by Ryskin & Leal (1984*a*) and Brabston & Keller (1975) for the inviscid bubble (the difference previously mentioned between the pressure at the surface found by Brabston & Keller 1975 and the present results has no severe consequences because it concerns mainly the symmetric part of P_s near the top

Re	0.1	0.2	0.5	1.0	5	10	20	100	200	300
Authors										
Stokes (1851)	240	120	48	24	—	—	—	—	—	—
	(160)	(80)	(32)	(16)						
Proudman & Pearson (1957)	244.5	124.5	52.5	28.5	—	—	—	—	—	—
	(163)	(83)	(35)	(19)						
Rimon & Cheng (1969)	—	—	—	—	—	4.398	—	1.014	0.727	0.610
Le Clair *et al.* (1970)	244.51	—	—	27.38	7.121	4.337	2.736	1.096	0.772	0.632
	(163.45)			(18.29)	(4.677)	(2.801)	(1.719)	(0.590)	(0.372)	(0.283)
Dennis & Walker (1971)	244.20	124.02	51.70	27.43	7.210	4.424	2.730	—	—	—
	(162.80)	(82.68)	(34.46)	(18.27)						
Present study	244.44	123.73	50.64	27.54	6.918	4.317	2.707	1.092	0.765	0.645
	(165.16)	(84.08)	(34.40)	(18.69)	(4.630)	(2.837)	(1.721)	(0.584)	(0.368)	(0.270)

TABLE 1. Drag coefficient of a rigid sphere in a uniform steady flow (when available the number in parentheses indicates the value of the friction drag coefficient)

Re	0.1	0.2	0.5	1.0	5	10	20	100	200	300
Authors										
Hadamard–Ribczynski (1911)	160	80	32	16	3.200	—	—	—	—	—
	(106.67)	(53.33)	(21.33)	(10.67)	(2.133)					
Taylor & Acrivos (1964)	162	82	34	18	5.2	—	—	—	—	—
	(108)	(54.67)	(22.67)	(12)	(3.467)					
Levich (1949, 1962)	—	—	—	—	9.600	4.800	2.400	0.480	0.240	0.160
					(6.400)	(3.200)	(0.160)	(0.320)	(0.160)	(0.107)
Moore (1963)	—	—	—	—	—	1.444	1.214	0.374	0.203	0.140
Brabston & Keller (1975)	161.66	—	33.70	17.59	4.368	2.350	1.362	0.375(*)	0.197	—
Ryvkind & Ryskin (1976)	—	—	33.80	17.50	—	2.430	1.410	—	—	—
Ryskin & Leal (1984*a*)	—	—	—	17.50	4.260	2.430	1.410	0.380	0.220	—
Oliver & Chung (1987)	—	—	33.80	17.60	—	2.480	1.430	—	—	—
Present study	161.80	82.18	33.76	17.44	4.266	2.411	1.322	0.369	0.200	0.138
	(103.26)	(52.40)	(21.52)	(11.42)	(2.692)	(1.544)	(0.801)	(0.233)	(0.127)	(0.088)

* Interpolated value

TABLE 2. Drag coefficient of an inviscid spherical bubble in a uniform steady flow (when available the number in parentheses indicates the value of the friction drag coefficient)

of the bubble). The results obtained for the rigid sphere confirm that the empirical drag law

$$C_D = \frac{24}{Re}\{1+0.15Re^{0.687}\} \tag{29}$$

often used in practical calculations involving rigid particles (see e.g. Clift *et al.* 1978) gives C_D with an error less than 6% in the whole range of Re covered by our investigation. Concerning the bubble it is worth noting that the asymptotic expression $C_D = 48Re^{-1}(1-2.21Re^{-1/2})$ given by Moore (1963) provides very accurate estimates for $Re \geqslant 50$. For $Re \leqslant 50$ our results are fitted with an accuracy better than 5% by the correlation

$$C_D = \frac{16}{Re}\{1+0.15Re^{0.5}\} \tag{30}$$

which matches Moore's expression at $Re = 50$. The ratio C_{VD}/C_D can be calculated from the results reported in tables 1 and 2. For the bubble this ratio varies from 0.64 at $Re = 0.1$ to the same value 0.64 at $Re = 300$. The creeping flow theory (Hadamard 1911; Ribczynski 1911) as well as the high-Reynolds-number theory (Kang & Leal 1988) give $C_{VD}/C_D = \frac{2}{3}$. Our results suggest that in the case of an inviscid bubble the relative contribution of pressure and viscous normal stress does not vary significantly with the Reynolds number. In contrast, for the rigid sphere the ratio C_{VD}/C_D varies from 0.67 at $Re = 0.1$ to 0.42 at $Re = 300$, meaning that the contribution of the pressure drag to the total drag of a rigid sphere becomes increasingly important with Re. This is a consequence of the nearly constant pressure found on the rear half of the sphere for $Re \geqslant 10$ and of the negative surface shear stress associated with the recirculating zone.

4. Stationary straining flow

4.1. *General considerations*

Stationary axisymmetric straining flow has been widely studied in the context of the deformation and breakup of drops and bubbles as it provides the essential ingredients leading to large deformations. Owing to the difficulties of the problem most of these studies have considered only creeping motions (see Rallison 1984 for a review). However, in the last decade a pioneering series of computations of bubble deformation at finite Reynolds numbers has been carried out: Ryskin & Leal (1984*b*) applied the numerical technique developed by Ryskin & Leal (1984*a*) to study bubble deformation in steady uniaxial straining flows. Some years later Kang & Leal (1987, 1989) generalized this approach to unsteady flows and studied both uniaxial and biaxial situations. The flow fields considered in all these works are symmetric with respect to the equatorial plane of the bubble so that no drag force exists. We are not aware of any numerical simulation of a steady axisymmetric straining flow around a non-deformable sphere. However, this flow represents a model of frequently encountered situations such as nozzles, sudden expansions or contractions and axisymmetric jets. Moreover the combination of a uniform stream with a steady axisymmetric straining flow represents the simplest situation in which, according to the results of Taylor (1928), Tollmien (1938), Voinov *et al.* (1973), Lhuillier (1982) and Auton *et al.* (1988), a sphere at rest experiences an added mass force caused by the spatial acceleration term $\boldsymbol{V}\cdot\boldsymbol{\nabla}\boldsymbol{V}$. All these theoretical results were obtained for an inviscid fluid. To check their validity in viscous flows and more generally to examine the combined effects of pure strain and

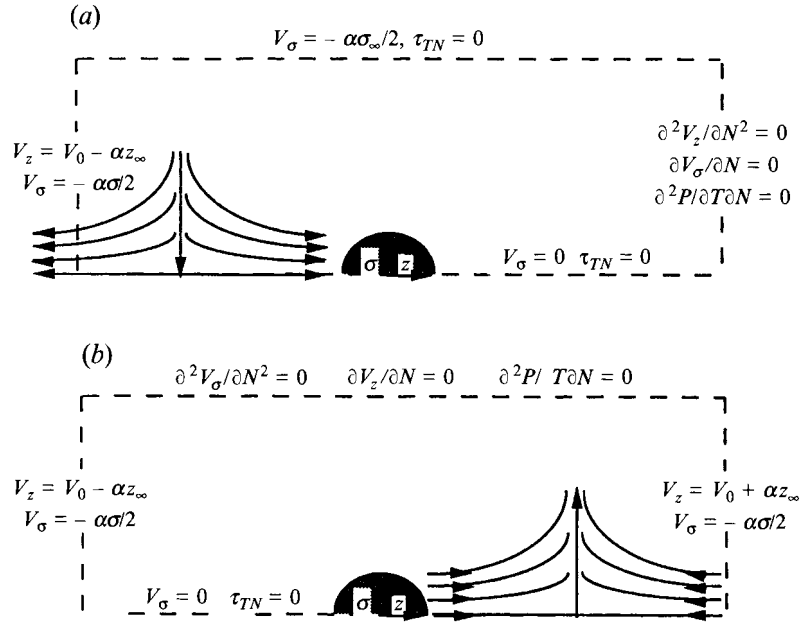

FIGURE 11. Steady axisymmetric straining flow: geometry and boundary conditions. (*a*) $\alpha > 0$, (*b*) $\alpha < 0$.

viscosity on the flow around a sphere the simplest axisymmetric straining flow has been selected. This basic flow is defined by

$$V_z(z) = V_0 + \alpha z, \quad V_\sigma(\sigma) = -\alpha\sigma/2. \tag{31a, b}$$

The flow around the sphere (whose centre is located at $z = \sigma = 0$) can be characterized by a Reynolds number and an acceleration number defined respectively by

$$Re_0 = V_0 D/\nu, \quad Ac = \alpha D/V_0. \tag{32a, b}$$

The acceleration number can be seen as the ratio between the acceleration due to the unperturbed flow (αV_0) and that due to the presence of the body (V_0^2/D). Note that according to definition (32*b*) the sign of the acceleration number changes with the sign of the strain for a given V_0.

In spite of its simplicity this flow is difficult to handle numerically: since α must be chosen large enough to produce significant effects on the sphere, V_z varies by more than one order of magnitude inside the computational domain $|z| \leqslant z_\infty$, $\sigma \leqslant \sigma_\infty$. Then owing to the large size of this domain a stagnation point exists. This point belongs to a plane where the streamwise velocity given by (31*a*) vanishes. For positive values of Ac this plane lies in the upstream part of the flow and the outer boundary conditions are chosen as shown in figure 11(*a*). In contrast when Ac is negative the flow is divergent and the stagnation point lies in the wake of the sphere. The outer boundary conditions are then chosen as indicated in figure 11(*b*). It is necessary to include the region where flow reversal occurs in the computational domain, especially when $Ac < 0$: if the size of the domain was reduced so as to keep $V_z(z)$ positive whatever $|z| \leqslant z_\infty$ an artificial confinement of the flow would be created for any significant value of Ac. Note that the unperturbed pressure distribution corresponding to (31*a*, *b*) is given by

$$P(z, \sigma) = P_0 - \rho\alpha V_0 z - \rho\alpha^2(\tfrac{1}{2}z^2 + \tfrac{1}{8}\sigma^2) \tag{33}$$

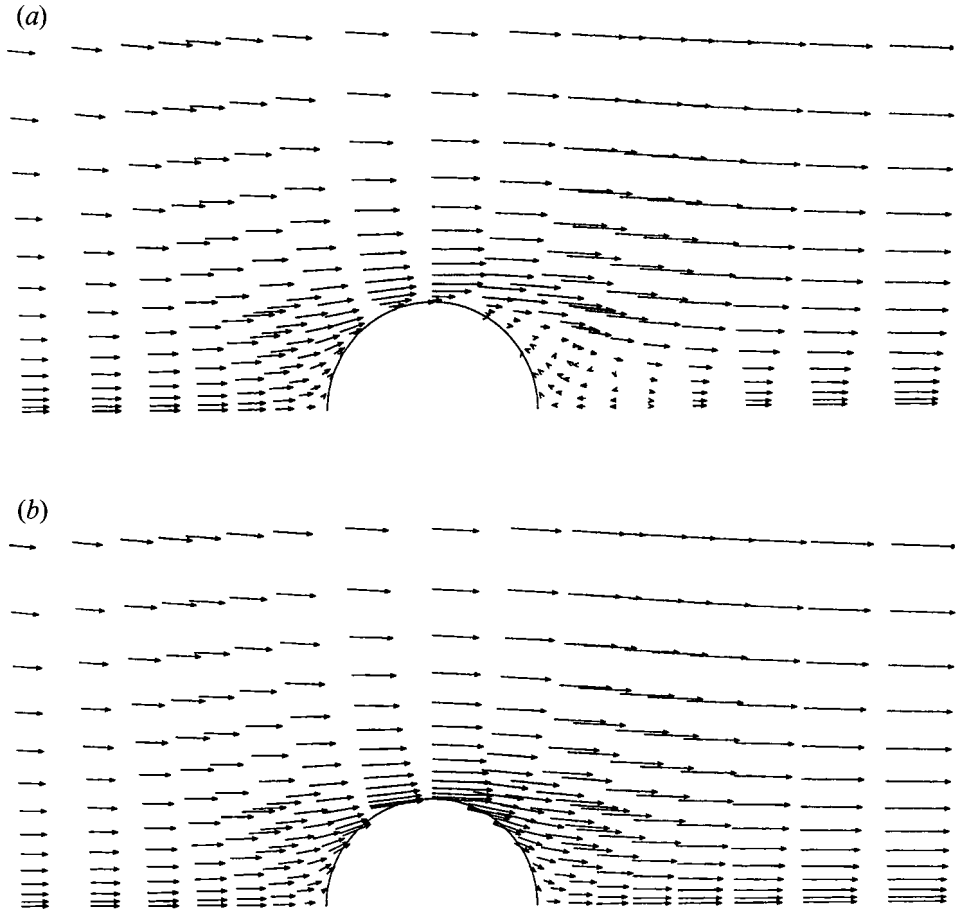

FIGURE 12. Velocity field around a sphere in a steady straining flow ($Re_0 = 300$, $Ac = 0.2$). (*a*) Rigid sphere, (*b*) inviscid bubble.

so that the outflow boundary conditions (19*a–c*) are all satisfied by the basic flow. Two different values of α leading to $|Ac| = 0.1$ or 0.2 are chosen ($|Ac| = 0.2$ corresponds for instance to a sphere of 1 mm of diameter rising or falling with a slip velocity $V_0 = 0.2$ m s^{-1} into a straining flow with $\alpha = 40$ s^{-1}). Even if the added mass effect is expected to be weak at low values of Re_0 the whole range $0.1 \leqslant Re_0 \leqslant 300$ is investigated to examine possible viscous effects.

4.2. *Flow characteristics for* $Ac > 0$

Figure 12(*a*, *b*) shows the velocity fields obtained for the two kinds of spheres at $Re_0 = 300$ and $Ac = 0.2$. These flow fields can be compared with those shown in figure 4. Owing to mass conservation the free-stream velocity is seen to increase very significantly from left to right. An important feature appears in the case of the rigid sphere: the separated region is much more reduced than in a uniform flow. This is a direct consequence of the existence of the favourable pressure gradient associated with a positive acceleration: the adverse pressure gradient usually found on the rear part of the sphere is reduced by this additional pressure gradient, delaying the formation of the separated region to larger angles. The influence of Ac on the evolution of the separation angle and reattachment length with Re_0 is shown in figure 13(*a*, *b*). First it

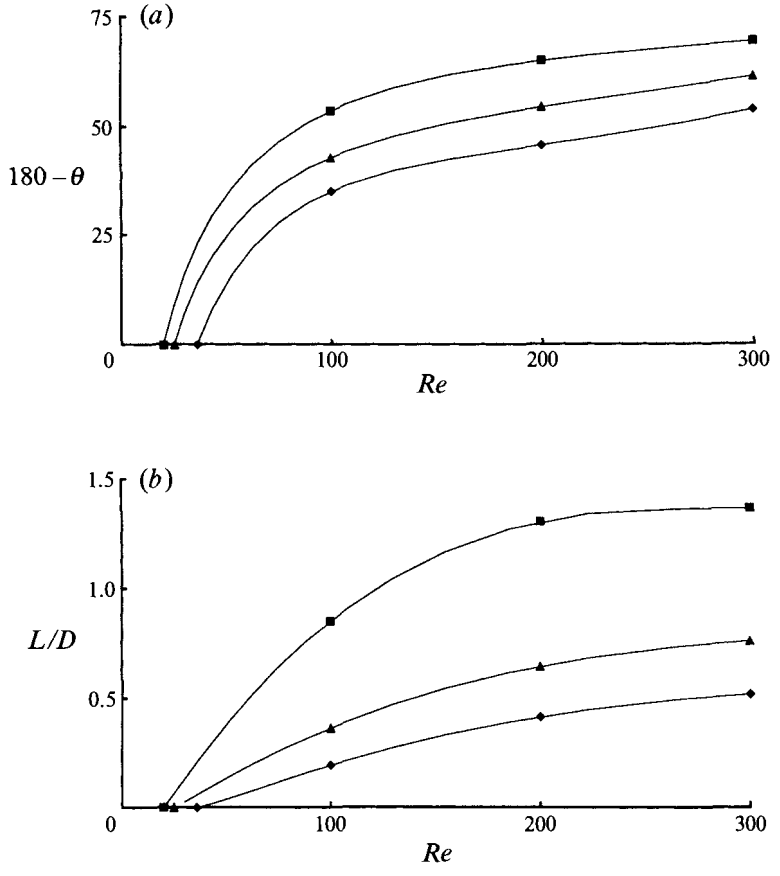

FIGURE 13. Influence of a positive strain on the characteristics of the separated region. (*a*) Separation angle, (*b*) reattachment length: ■, $Ac = 0$; ▲, $Ac = 0.1$; ◆, $Ac = 0.2$.

can be noted that the critical Reynolds number at which separation occurs is found to increase from the well-known value $Re \approx 20$ in uniform flow to $Re_0 \approx 25$ for $Ac = 0.1$ and $Re_0 \approx 36$ for $Ac = 0.2$. Figure 13(*a*, *b*) also confirms that the separated region is dramatically reduced when Ac is positive (see figure 9*a*, *b* for comparison). For example at $Re_0 = 100$ and $Ac = 0.2$, separation occurs at $\theta \approx 145.2°$ while the flow reattaches very near the sphere at $L/D \approx 0.19$.

Since separation at the surface of a non-deformable body is associated with a change of sign of vorticity, the modifications found in the separated region indicate that the presence of the strain changes the distribution of vorticity around the sphere. These changes result from two different mechanisms.

First, additional vorticity is generated at the surface of the sphere because the straining flow must satisfy the no-slip or shear-free boundary condition. With respect to uniform flow the existence of the strain modifies the distance between two given streamlines: for a positive value of Ac this distance is smaller on the rear half of the body and larger on the fore half. Thus velocity gradients at the surface of the sphere are decreased for $\theta < \frac{1}{2}\pi$ and increased for $\theta > \frac{1}{2}\pi$ (recall that θ increases clockwise as indicated in figure 2). One can thus expect the no-slip boundary condition to cause an increase of vorticity for $\theta > \frac{1}{2}\pi$ and a reduction for $\theta < \frac{1}{2}\pi$. In the case of a bubble, the vorticity at the surface is directly proportional to the tangential velocity. Since for a

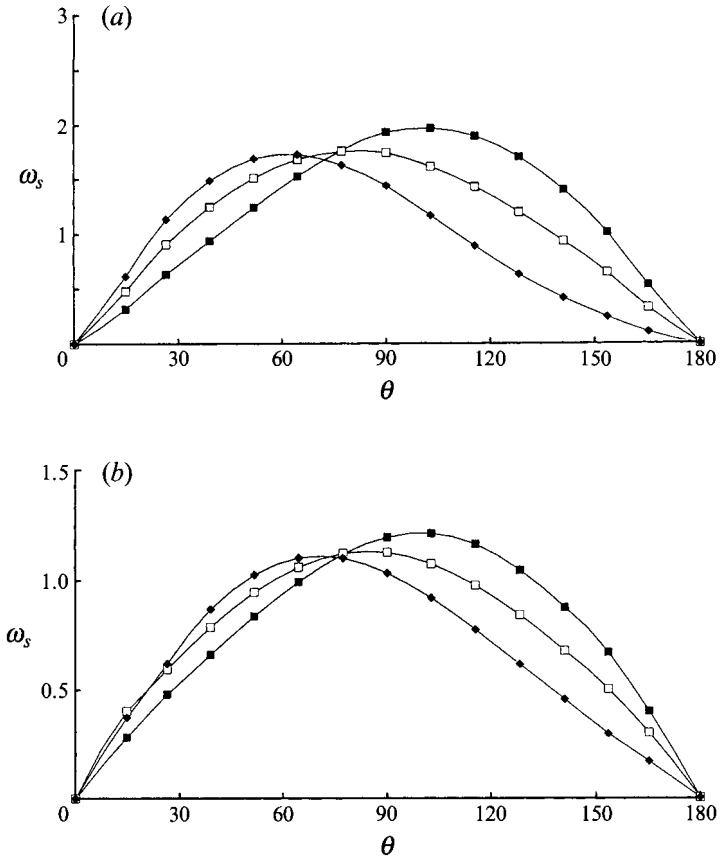

FIGURE 14. Influence of the strain on the surface vorticity; $Re_0 = 1$. (*a*) Rigid sphere, (*b*) inviscid bubble: ■, $Ac = 0.2$; □, $Ac = 0$; ◆, $Ac = -0.2$.

positive Ac the velocity increases along a streamline, the tangential velocity at a given location of the rear half of the bubble is larger than at the symmetric location of the fore half. Thus, as for the rigid sphere, vorticity increases for $\theta > \frac{1}{2}\pi$ and decreases for $\theta < \frac{1}{2}\pi$. This can be confirmed by considering the limit for high Reynolds number of the straining viscous flow around an inviscid bubble. At leading order in Re^{-1} the non-dimensional solution is given by the velocity potential:

$$\phi(r_a, \theta) = -\left(r_a + \frac{1}{2r_a^2}\right)\cos\theta + \frac{Ac}{24}\left(\frac{3}{2}r_a^2 + \frac{1}{r_a^3}\right)(1 + 3\cos 2\theta), \tag{34}$$

where velocities have been scaled by V_0 and distances by the bubble radius $\frac{1}{2}D$. The velocity field derived from (34) generates a non-zero shear stress at the surface of the bubble. The zero-shear-stress boundary condition (24*a*) is then satisfied by adding a rotational correction given by

$$\omega(r_a = 1, \theta) = \{3\sin\theta - \tfrac{5}{4}Ac\sin 2\theta\}. \tag{35}$$

The last term in (35) is due to the existence of the strain and behaves as expected from the previous discussion. Figures 14(*a*, *b*) and 15(*a*, *b*) show the influence of the strain rate on the surface vorticity at $Re_0 = 1$ and 300 for both the rigid sphere and the bubble. They confirm the foregoing conclusions concerning the decrease of ω for $\theta < \frac{1}{2}\pi$ and its increase for $\theta > \frac{1}{2}\pi$. Figure 15(*a*, *b*) shows that an important difference exists

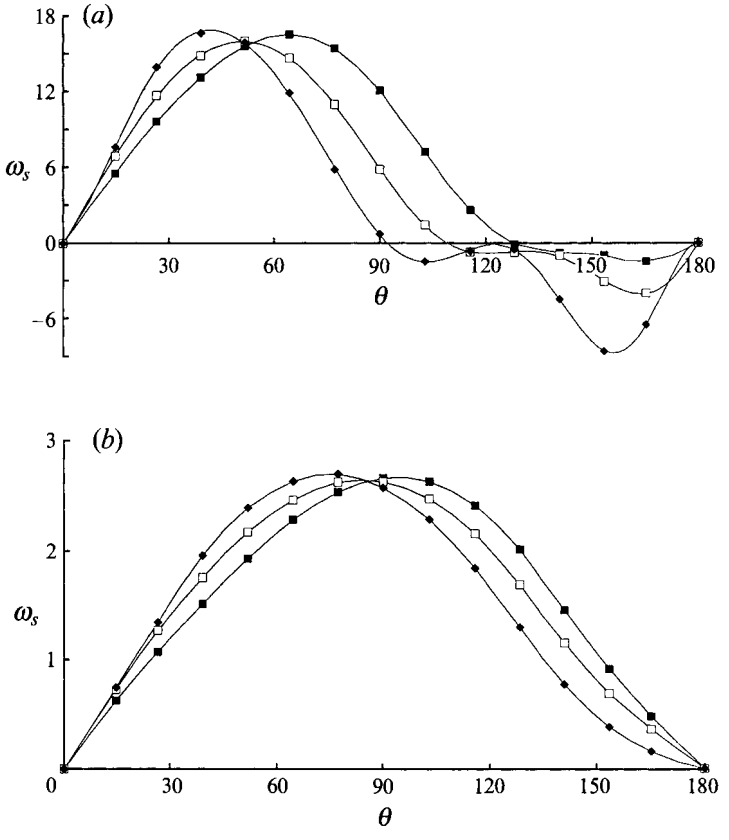

FIGURE 15. As figure 14, but for $Re_0 = 300$.

between the inviscid bubble and the rigid sphere at high Reynolds number: while the effect of the strain has the same magnitude on the two halves of the bubble, as predicted by (35), it is much more important on the rear half of the rigid sphere than on its fore half. As discussed below, this asymmetry has important consequences for the drag of the rigid sphere.

The second mechanism leading to changes in the vorticity distribution is related to vorticity balance. Since the streamlines of the straining flow are different from those of a uniform flow, vorticity balance implies a modification of vorticity gradients. However, this modification is not completely intuitive: a vortex-stretching mechanism which has no counterpart in uniform flow exists in the flow field (31*a*, *b*). The streamlines $\Psi = \text{const.}$ corresponding to the velocity field (31*a*, *b*) are given in non-dimensional form by

$$\sigma_a(z_a) = \left(\frac{4\Psi}{2 + Ac\, z_a}\right)^{1/2}. \tag{36}$$

Far from the sphere viscous diffusion is negligible and vorticity obeys the Helmholtz equation (Batchelor 1967):

$$\frac{\mathrm{D}(\omega/\sigma)}{\mathrm{D}t} = 0. \tag{37}$$

It is thus clear that, outside the domain where viscous effects are important, vorticity that has been created at the surface of the sphere does not remain constant along a streamline as in uniform flow but varies according to (36) and (37). When Ac is positive

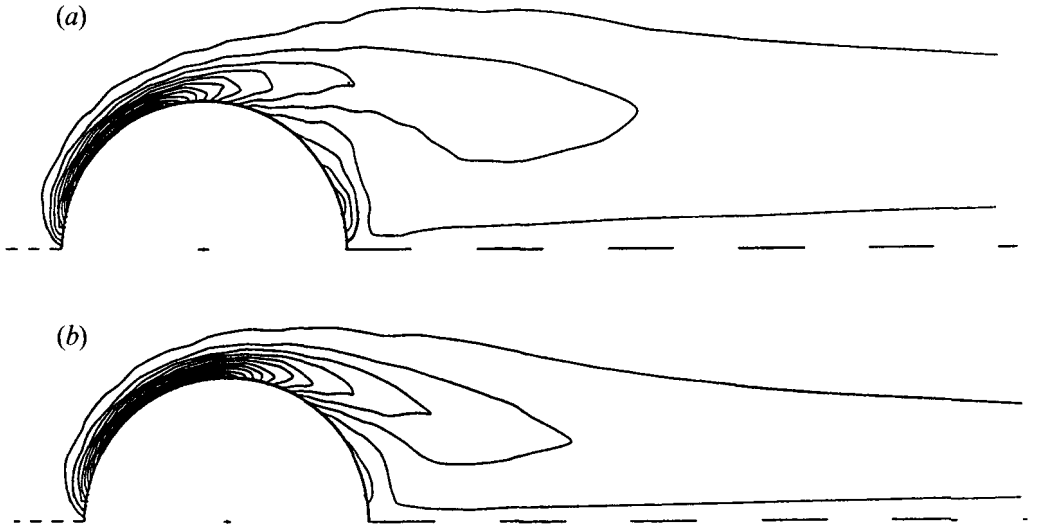

FIGURE 16. Influence of the strain on the vorticity field around a rigid sphere; $Re_0 = 300$. (*a*) Uniform flow ($Ac = 0$); $\Delta\omega = 1.0$, (*b*) straining flow ($Ac = 0.2$); $\Delta\omega = 1.0$.

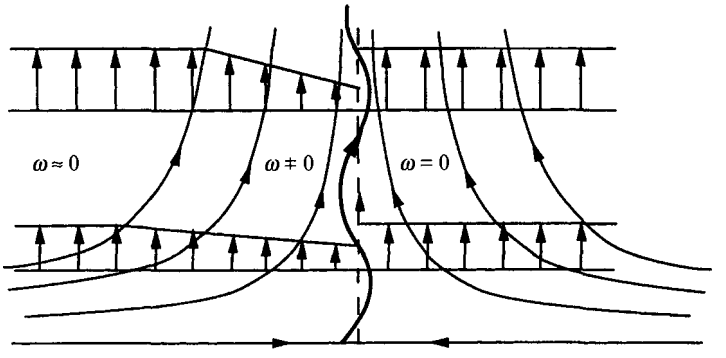

FIGURE 17. The instability mechanism of the biaxial straining flow ($Ac < 0$).

(uniaxial straining) $\mathrm{d}\sigma/\mathrm{d}z$ is negative and vorticity decreases as the fluid moves downstream in the wake. The combined effects of transport, stretching and diffusion on vorticity distribution near the sphere can be appreciated in figure 16(*b*) and compared to the uniform situation in figure 16(*a*). The effect of the contraction of the streamlines at the rear of the sphere appears clearly: in the wake the isovorticity contours are deflected towards the symmetry axis. As a consequence the region of the flow containing significant vorticity is more confined near the sphere than in a uniform flow.

4.3. *Flow characteristics for* $Ac < 0$

Following the sign of Ac, the vortex-stretching mechanism previously described leads to two different types of behaviour as already pointed out by Kang & Leal (1989) and Leal (1989) for the case $V_0 = 0$. In contrast with what happens when Ac is positive, in flows where Ac is negative (biaxial straining) (36) and (37) show that vorticity generated at the surface of the sphere increases along the streamlines and tends to become infinite along the stagnation plane $z_a = -2/Ac$. At the same time streamlines coming from the 'downstream' boundary $z_a = z_{a_\infty}$ do not carry any vorticity (see figure 17) and reach the plane $z_a = -2/Ac$ with $\omega = 0$ (actually the plane is no longer exactly located at $z_a = -2/Ac$ in the presence of vorticity on one side because the continuity

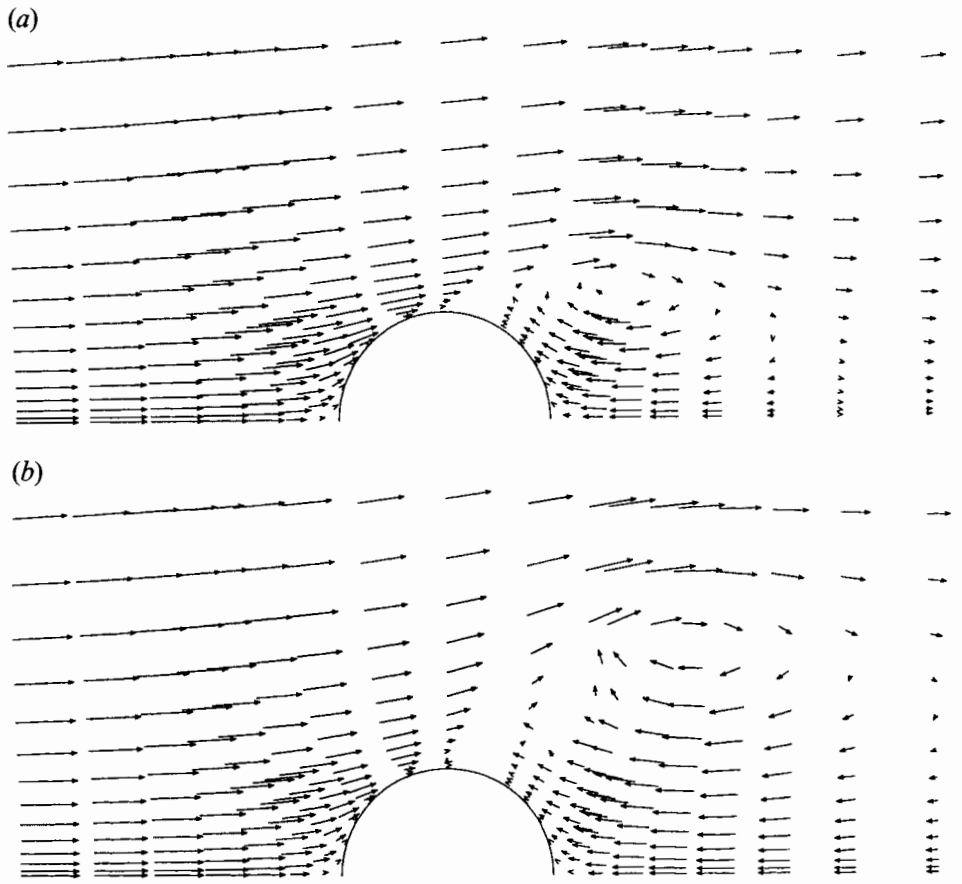

FIGURE 18. The biaxial straining flow around a rigid sphere at two different times; $Re_0 = 300$, $Ac = -0.2$. (a) $t \approx 1.2|Ac^{-1}|$, (b) $t \approx 2.4|Ac^{-1}|$.

of the pressure across the plane implies a slightly different location). A fundamental question concerns the matching between the two parts of the flow and the real possibility of observing such a flow. Clearly a large diffusion of vorticity across the plane $z_a = -2/Ac$ is needed to maintain the compatibility between the two regions. Is viscous diffusion sufficiently efficient whatever Re_0 to ensure this matching? The computations carried out in the range $0.1 \leqslant Re_0 \leqslant 300$ with $Ac = -0.2$ and -0.1 lead to a steady solution only for relatively low values of Re_0. For larger Re_0 the flow is found to be unstable and an unsteady solution develops. In such cases examination of the velocity and pressure fields after the onset of the instability shows that no numerical perturbation exists near the outer boundaries: the instability comes undoubtedly from the region of the stagnation plane. To ensure that the specific effects occurring in that region are correctly captured (especially those related to viscosity) the mesh has been stretched there, leading to the conclusion that the characteristics of the instability are mesh independent.

Actually this instability is of Kelvin–Helmholtz type. Its basic mechanism can be summarized as follows. Owing to the enhancement of the vorticity by the vortex stretching mechanism a substantial amount of vorticity reaches the stagnation region. Thus in that region the velocities of the fluid elements coming from the sphere differ from those of the stream coming from the boundary $z_a = z_{a_\infty}$. In particular, compared

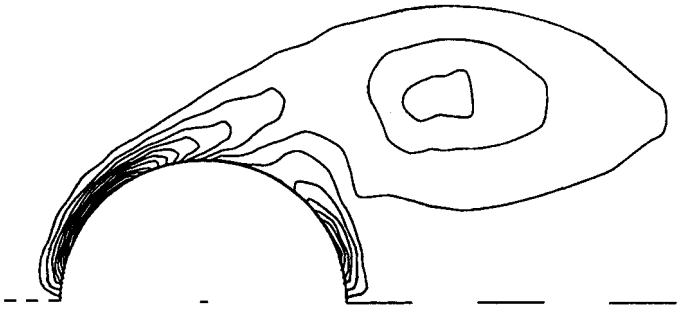

FIGURE 19. The vorticity field around a rigid sphere in the presence of a negative strain; $Re_0 = 300$, $Ac = -0.2$, $t \approx 1.2t_i$; $\Delta\omega = 1.0$.

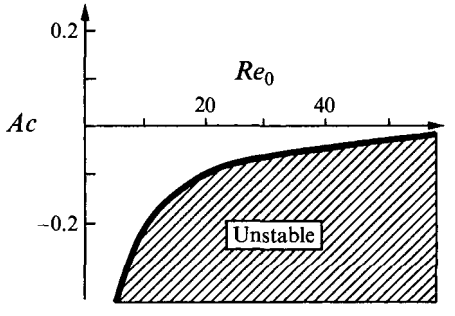

FIGURE 20. Stability domain of the axisymmetric straining flow around a sphere (qualitative diagram).

to the potential flow (31*a*, *b*) the radial velocities V_σ are decreased by the positive vorticity generated at the surface of the sphere. Thus the tangential velocity (with respect to the stagnation plane) V_σ experiences a jump across this plane (figure 17). Since ω increases with σ so does the jump. This jump can be spread by viscosity at low values of Re_0 but it leads necessarily to an instability beyond a critical value of Re_0. After the onset of the instability the stagnation plane deforms in a wavy surface and perturbations develop on both sides in the velocity field.

Figure 18(*a*, *b*) depicts two stages of this unstable flow for the case of a rigid sphere. In figure 18(*a*) vorticity has not yet reached the stagnation region (this requires a non-dimensional time $t_i \approx 2|Ac|^{-1}$). Note that the separated region is already very well developed and that the centre of the vortex is located very high above the symmetry axis. In figure 18(*b*) the instability has developed. The vortex now fills almost the entire wake up to $z_a = -2/Ac$ and more than half of the sphere experiences a negative shear stress. The vortex oscillates and goes on growing above the sphere. In later stages secondary vortices are shed near the top of the sphere. Figure 19 shows the vorticity field corresponding to the velocity field of figure 18(*a*). The effect of the vortex-stretching mechanism is clearly illustrated by the isovorticity contours at the rear of the sphere. Owing to viscosity the vorticity produced at the surface first diffuses and decays. Then when vorticity begins to be advected downstream the vortex stretching starts to act and increases the vorticity in the near wake as shown by the occurrence of a local maximum.

The stability domain of the flow can be determined by carrying out computations for a given negative value of Ac at several values of Re_0 and monitoring the evolution of velocity variations throughout the simulation. A qualitative map of this stability domain in the range $1 \leqslant Re_0 \leqslant 60$ for both a rigid sphere and a bubble is shown in

figure 20: with $Ac = -0.2$ the flow becomes unsteady for $Re_0 > 10$ while the limit is $Re_0 \approx 20$ for $Ac = -0.1$. For a given value of Ac the instability occurs at nearly the same critical Reynolds number for both a rigid sphere and a bubble: near the stagnation plane the stabilizing effect of viscosity is basically governed by the potential flow (31 *a*, *b*) which is independent of the nature of the body and a small amount of vorticity in that region is sufficient to destabilize the flow whatever its origin.

It is interesting to note that in the present situation the physical behaviour of the flow near the stagnation plane is completely different from that described by Kang & Leal (1989). Those authors examined a symmetric biaxial straining flow in which the stagnation plane is necessarily located at $z_a = 0$. In that case vorticity comes from both sides of the plane with opposite signs. Since symmetry on that plane is enforced by imposing $\omega = 0$ and computing only half of the flow no instability can occur on the position of the stagnation surface. Thus the question solved by Kang & Leal (1989) is that of the matching between a non-zero vorticity growing with σ near $z_a = 0$ and the condition $\omega = 0$ on the plane itself. The authors showed by a boundary layer analysis that the large gradient of vorticity along the direction z, normal to the symmetry plane, enables viscosity to match a steady solution to the symmetry condition whatever the Reynolds number. This striking difference with the situation described by the present computations highlights the sensitivity of the biaxial straining flow to asymmetric conditions.

The limited extent of the stability domain shown in figure 20 implies *a priori* that the applicability of steady results obtained for the hydrodynamic force in diverging flows is reduced to a narrow range of values of Re_0. Nevertheless, whatever its fundamental interest the situation examined here is rather academic: in real configurations, diverging (or converging) flows are generally encountered over regions of limited extent and no general reversal of the flow is observed since the fluid is blown along a given direction, the diverging or converging effect being obtained by a suitable form of the walls. In such cases the instability previously discussed does not appear (however the flow is certainly less stable than its uniform counterpart). Such a configuration involves a new parameter, namely the ratio λ between the sphere radius and the distance from the centre of the sphere to the downstream end of the diverging region. If λ is small, one can expect the flow near the sphere and hence the hydrodynamic force to be nearly independent of λ. Some results of present computations can be used as an approximation of the hydrodynamic force in a real steady diverging flow with small λ in the following way. As previously mentioned, instability occurs in the biaxial straining flow after vorticity has reached the stagnation plane, i.e. for $t > t_i$. In the present computations the stagnation plane lies between 10 and 20 radii downstream of the sphere. If viscous effects around the sphere extend over a characteristic length δ these effects reach a steady state within a time $t_v \approx \delta^2/\nu$. If $\delta/D \ll 1$ the time t_i is sufficient to enable the flow to reach nearly its steady state. In the present study this is indeed the case for the bubble, owing to the values of the various parameters. Values of the drag parameters recorded at $t = t_i$ just before the instability occurs can thus be considered as a good estimate of their value in a really steady diverging flow corresponding to a small λ. For that reason these values will be termed hereafter 'nearly steady' values. In contrast for the rigid sphere $\delta/D = O(1)$ and the separated region has not time to develop completely. Thus in that case no complete conclusion can be drawn from the value of the drag coefficients at $t = t_i$ and such values will be termed 'non-developed'.

As can be expected the effects of the deceleration ($Ac < 0$) on the flow near the sphere are qualitatively opposite to those found with $Ac > 0$. The vorticity at the

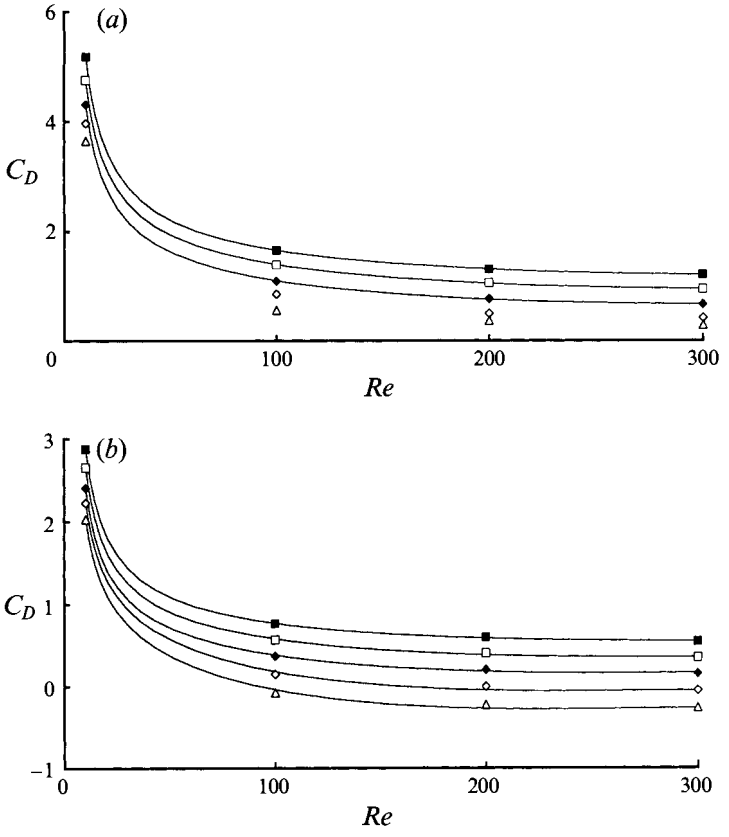

FIGURE 21. Evolution of the total drag coefficient with Reynolds number in a straining flow. (*a*) Rigid sphere (no fitting is proposed for $Ac < 0$ since the values of C_D do not correspond to a steady state), (*b*) Inviscid bubble: ■, $Ac = 0.2$; □, $Ac = 0.1$; ◆, $Ac = 0$; ◇, $Ac = -0.1$; △, $Ac = -0.2$.

surface increases on the fore half of the sphere and decreases on the rear half (figures 14*a*, *b* and 15*a*, *b*). In the case of the rigid sphere, even if no steady state is reached, it is obvious that the separation angle is strongly reduced while the reattachment length increases dramatically (figure 18*a*). Furthermore the deceleration severely reduces the critical Reynolds number at which separation occurs: the flow separates at $Re_0 = 7.8$ for $Ac = -0.1$ and at $Re_0 = 3.3$ for $Ac = -0.2$!

4.4. *The total drag*

The results concerning the drag force are expressed within the form of generalized drag coefficients C_D, C_{VD} and C_{PD} defined according to (27) and (28) by replacing V_∞ by $V(0,0) = V_0 \boldsymbol{e}_z$. The evolution of C_D and C_{PD} with Re_0 and Ac is shown for $Re_0 \geqslant 10$ in figures 21(*a*, *b*) and 22(*a*, *b*) respectively. At low Reynolds numbers the influence of Ac is weaker: at $Re_0 = 0.1$, C_D changes by less than 4% for $|Ac| = 0.2$. This is the reason why the evolution of the coefficients is not shown for $Re_0 < 10$. Nevertheless the values of C_D and C_{VD} obtained in the whole range $0.1 \leqslant Re_0 \leqslant 300$ are reported in tables 3 and 4. At moderate and high Reynolds numbers the two coefficients C_D and C_{PD} experience considerable variations with Ac. In particular it is interesting to notice that in a diverging flow with $Ac = -0.2$ (resp. -0.1) the nearly steady drag obtained for a bubble at $Re_0 \geqslant 100$ (resp. $\geqslant 200$) is negative, meaning that the total drag is in the direction opposite to the flow. This emphasizes the dominant role of pressure effects

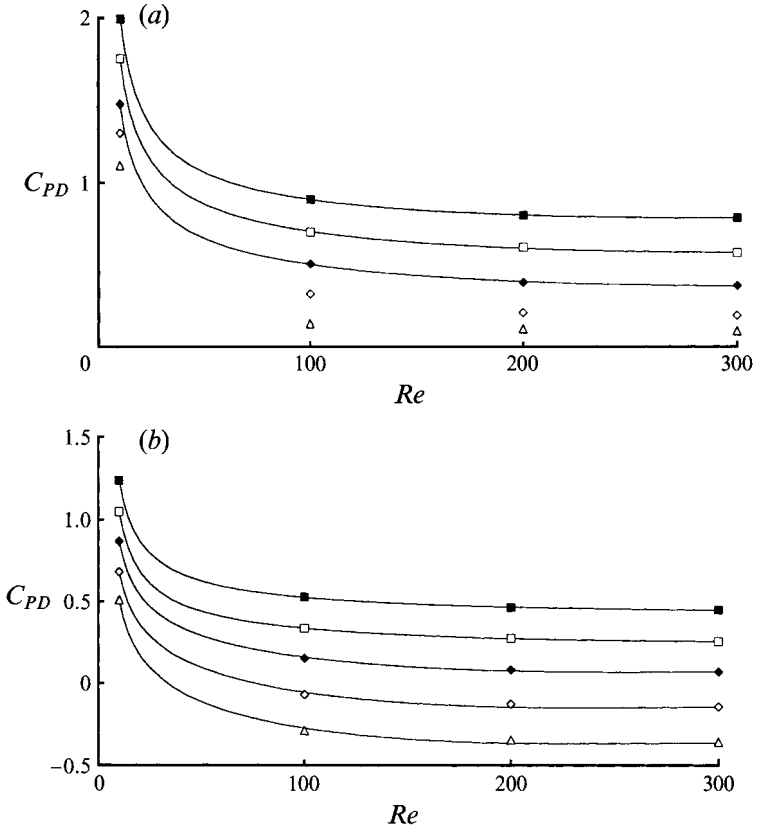

FIGURE 22. As figure 21 but for the evolution of the pressure drag coefficient.

Re	0.1	1	10	100	200	300
Ac						
0.1	250.00	28.78	4.750	1.387	1.057	0.924
	(169.16)	(19.35)	(2.997)	(0.689)	(0.446)	(0.346)
0.2	254.14	30.10	5.182	1.655	1.304	1.189
	(171.88)	(20.15)	(3.189)	(0.755)	(0.498)	(0.399)
−0.1	237.66	24.18	3.972	0.853^{ND}	0.497^{ND}	0.406^{ND}
	(160.86)	(16.40)	(2.667)	$(0.323)^{ND}$	$(0.285)^{ND}$	$(0.209)^{ND}$
−0.2	233.97	22.65	3.649	0.557^{ND}	0.366^{ND}	0.272^{ND}
	(158.56)	(15.44)	(2.542)	$(0.416)^{ND}$	$(0.252)^{ND}$	$(0.173)^{ND}$

ND: non-developed state.

TABLE 3. Generalized drag coefficient C_D of a rigid sphere in a straining flow (the number in parentheses indicates the generalized friction drag coefficient C_{VD})

related to Ac on the total drag as the Reynolds number increases. To analyse more precisely the influence of Ac it is necessary to consider separately viscous and pressure contributions: since the theoretical result given by (1) was derived for inviscid flows, the corresponding effects must be contained in C_{PD}. In other words if the only effect of the strain rate were to induce the inertia force given by (1) the results should be

$$C_{VD}(Re_0, Ac) = C_{VD}(Re_0, 0), \quad C_{PD}(Re_0, Ac) = C_{PD}(Re_0, 0) + \tfrac{4}{3}(1 + C_M)\, Ac, \quad (38a, b)$$

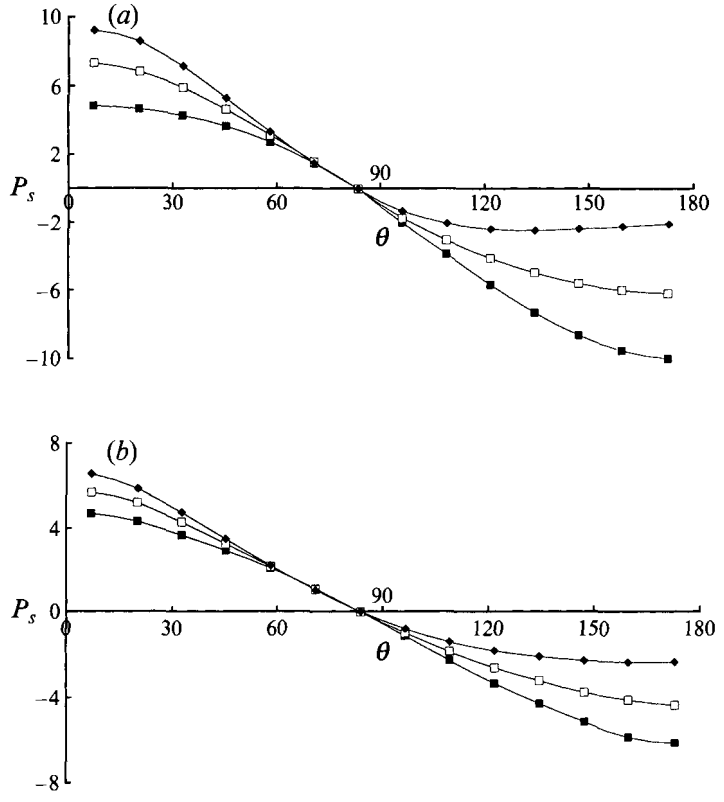

FIGURE 23. Influence of the strain on the surface pressure. $Re_0 = 1$. (The reference pressure is defined at a different location for each Ac so that the values of P_s have comparable magnitude). (*a*) Rigid sphere, (*b*) inviscid bubble: ■, $Ac = 0.2$; □, $Ac = 0$; ◆, $Ac = -0.2$.

Re	0.1	1	10	100	200	300
Ac						
0.1	163.58	18.07	2.657	0.565	0.396	0.335
	(104.73)	(11.46)	(1.609)	(0.230)	(0.124)	(0.086)
0.2	165.41	18.66	2.880	0.762	0.589	0.530
	(105.81)	(11.75)	(1.641)	(0.235)	(0.125)	(0.087)
−0.1	155.73	16.19	2.230	0.150^{NS}	-0.006^{NS}	-0.063^{NS}
	(101.83)	(10.75)	(1.548)	$(0.219)^{NS}$	$(0.121)^{NS}$	$(0.085)^{NS}$
−0.2	154.10	15.76	2.035	-0.075^{NS}	-0.225^{NS}	-0.278^{NS}
	(100.84)	(10.43)	(1.523)	$(0.210)^{NS}$	$(0.118)^{NS}$	$(0.084)^{NS}$

^{NS}: nearly steady state.

TABLE 4. Generalized drag coefficient C_D of an inviscid spherical bubble in a straining flow (the number in parentheses indicates the generalized friction drag coefficient C_{VD})

where $C_{VD}(Re_0, 0)$ and $C_{PD}(Re_0, 0)$ stand for the viscous and pressure drag coefficients found in uniform flow at the same Reynolds number Re_0. Expressions (38) suggest expanding linearly the various coefficients with respect to Ac with the aid of a least-square fit. Naturally from the point of view of accuracy such an expansion is realistic only if Ac is not too small compared to C_{PD}. Furthermore this procedure is not fully satisfactory since it has been shown previously that according to the sign of Ac the flows exhibit some markedly different properties. Such an overall method cannot account for

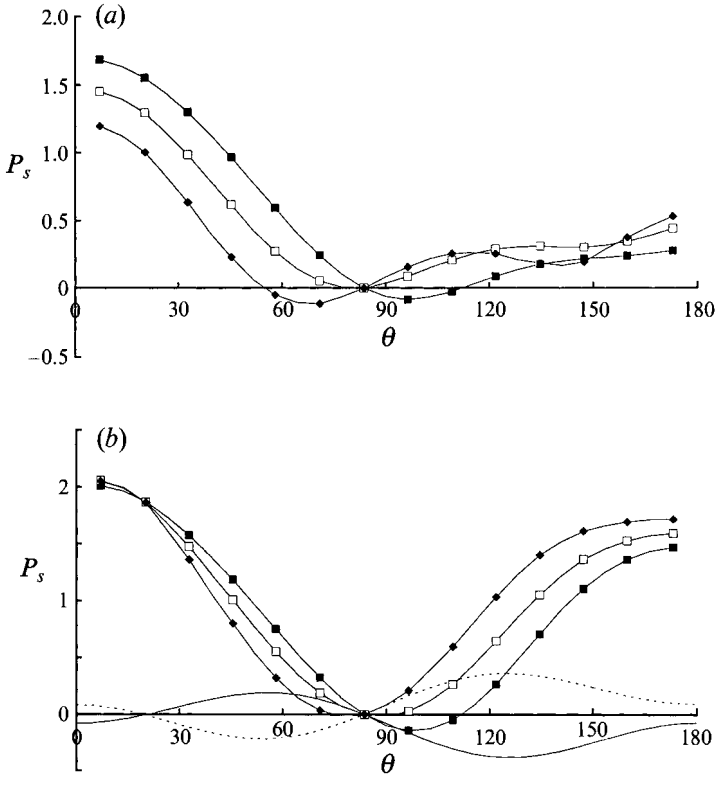

FIGURE 24. As figure 23 but for $Re_0 = 300$. In (b) influence of Ac (potential theory): ——, $Ac = 0.2$; – – –, $Ac = -0.2$.

all the effects linked to the distribution of vorticity but it provides the only way to obtain the general tendencies of the evolution of the drag coefficients. For $Re_0 \geqslant 10$ this method works well and an accurate fitting of the steady or 'nearly steady' results is given by

$$C_{PD}(Re_0, Ac) = (1+0.17Ac)\,C_{PD}(Re_0, 0)+1.96Ac, \tag{39a}$$

$$C_{VD}(Re_0, Ac) = (1+0.35Ac)\,C_{VD}(Re_0, 0)+0.57Ac, \tag{39b}$$

for the rigid sphere, and

$$C_{PD}(Re_0, Ac) = (1-0.25Ac)\,C_{PD}(Re_0, 0)+2.04Ac, \tag{40a}$$

$$C_{VD}(Re_0, Ac) = (1+0.19Ac)\,C_{VD}(Re_0, 0) \tag{40b}$$

for the inviscid bubble. These results differ significantly from the behaviour depicted by (38a, b). The reason for this is that the strain induces not only an inertia force but also a modification of the viscous drag which is a direct consequence of the changes found in the vorticity distribution.

4.5. *The pressure drag and the inertia force*

As shown before the distribution of pressure imposed by the straining flow plays a central role in the drag experienced by the sphere. This role is easily seen in figures 23(a, b) and 24(a, b) which present the distribution of the surface pressure P_s for $Re_0 = 1$ and 300 respectively at various values of Ac: the acceleration induced by the strain results in an asymmetry of the surface pressure with respect to the plane

$\theta = \frac{1}{2}\pi$ and thus contributes to the total drag. At high Reynolds number the pressure distribution on the inviscid bubble can be explained by looking at the potential solution. Using the velocity potential (34), the Bernoulli equation gives the pressure distribution at the surface of the sphere as

$$P_a(r_a = 1, \theta) = -\tfrac{9}{4}\sin^2\theta + \tfrac{5}{8}(3Ac\sin\theta - \tfrac{5}{8}Ac^2\sin 2\theta)\sin 2\theta + \text{const.} \tag{41}$$

The first term on the right-hand side in (41) is the pressure distribution in uniform flow plotted in figure 8(*c*). The two last terms represent the contribution of the acceleration induced by the strain and are plotted in figure 24(*b*) using the same reference pressures as for P_s. The second term results in both the added mass force and the buoyancy force induced by the pressure gradient of the undisturbed straining flow and thus leads to the last term of (38*b*). Figure 24(*b*) suggests that (41) describes accurately the evolution of the pressure at the surface of the bubble. The situation for the rigid sphere appears much more complex. Figure 24(*a*) shows that on the front half P_s experiences an important shift which cannot be explained by (41): a large part of this shift results from the distribution of vorticity imposed by the strain. On the rear half the presence of the recirculating zone reduces the variations of P_s but in the case $Ac = 0.2$ the evolution of P_s follows roughly the same tendencies as the potential solution (the case $Ac = -0.2$ is not fully developed and the evolution of P_s on the rear half of the sphere reflects this situation). At low Reynolds number (see figure 23*a*, *b*) the strain also results in an additional asymmetry of P_s which has the same form for both a rigid sphere and an inviscid bubble. However, as could be expected, this asymmetry does not follow (41).

We turn now to the determination of the added mass coefficient. Identifying the last term of correlations (39*a*) and (40*a*) with the term $\frac{4}{3}(1 + C_M)Ac$ of (38*b*) gives the approximate values $C_M = 0.47$ and $C_M = 0.53$ for the rigid sphere and the inviscid bubble respectively. Since the overall relative accuracy of the calculations can be estimated to 0.5% and since in the present situations added mass represents between 1.5% and 11% of the total force for the rigid sphere (between 2.7% and 25% for the bubble), the accuracy of C_M is not very high (it can be estimated approximately as 8% and 4% for the rigid sphere and the bubble respectively). Taking into account these limitations the two values previously mentioned appear remarkably close to the theoretical result $C_M = \frac{1}{2}$. It can thus be concluded from these results that (1) with $C_M = \frac{1}{2}$ holds for viscous flows. These conclusions prove the concept of added mass to be relevant for non-uniform viscous flows and confirm unambiguously that the added mass force involves the acceleration of the fluid $\mathrm{D}\boldsymbol{V}/\mathrm{D}t$: if instead of $\mathrm{D}\boldsymbol{V}/\mathrm{D}t$ the added mass involved the derivative of $\boldsymbol{V}$ following the sphere, i.e. $\mathrm{d}\boldsymbol{V}/\mathrm{d}t = \partial\boldsymbol{V}/\partial t + \boldsymbol{V}_P\cdot\boldsymbol{\nabla}\boldsymbol{V}$ we should get no added mass effect in present computations since $\boldsymbol{V}_P = \boldsymbol{0}$. Furthermore the present results, which have been obtained using values of Ac frequently encountered in real situations, show quantitatively that at moderate or high Reynolds numbers trajectories of bubbles or rigid particles embedded in non-uniform flows (and especially in turbulent flows) cannot be accurately determined without taking into account the inertia force caused by the spatial acceleration $\boldsymbol{V}\cdot\boldsymbol{\nabla}\boldsymbol{V}$.

4.6. *The viscous drag*

Let us now consider the second effect of the strain shown by previous results, namely the modification of the viscous drag (including the part of C_{PD} due to viscosity). Vorticity at the surface of a rigid sphere is an $O(Re^{1/2})$ quantity whereas it is $O(1)$ for an inviscid bubble. One can thus expect the influence of Ac on the total drag via viscous effects to be much weaker for the inviscid bubble than for the rigid sphere. This is confirmed by comparing correlations (39*b*) and (40*b*). Moreover correlations (40*a*, *b*)

show that for a bubble Ac tends to increase C_{VD} and to decrease C_{PD} by nearly the same amount. This results in a small effect on the global drag coefficient C_D which never goes beyond 1.5% in our simulations. These conclusions for the inviscid bubble agree qualitatively with those that can be drawn from the velocity potential (34). Equation (35) shows how the vorticity at the surface of the sphere is modified by the strain when the Reynolds number is large. It can be proved that the supplementary term results in an even contribution to surface pressure distribution and thus does not modify C_{PD} (see Kang & Leal 1988 for the determination of surface pressure from vorticity). A similar result can be obtained for the normal stress contribution derived from (34). At leading order in Re^{-1} it yields

$$\tau_{NN}(r_a = 1, \theta) = (4/Re)\{-6\cos\theta + \tfrac{5}{4}Ac(1 + 3\cos 2\theta)\}. \tag{42}$$

The additional term appearing in (42) is even, so that $C_{VD}(Re_0, Ac) = C_{VD}(Re_0, 0)$. Thus, at very high Reynolds number, asymptotic theory shows that an inviscid bubble does not undergo any viscous modification due to the strain. This conclusion can be qualitatively extended to lower Reynolds numbers since the form of the distributions of surface vorticity and normal stress remains nearly the same whatever Re. Consequently in the case of a bubble it is likely that only minor modifications of the viscous drag will be found within the nearly the whole range of Re (the most significant change is found at the intermediate value $Re_0 = 10$ where the vorticity at the surface exhibits the maximal asymmetry as shown by figure 6*a*).

Conclusions concerning the rigid sphere are markedly different. The values reported in table 3 as well as the correlation (39*b*) show that C_{VD} is strongly influenced by the strain when $Re_0 \geqslant 10$. This can be related to the evolution of the shape of the surface vorticity distribution: at low Reynolds number this distribution is nearly symmetric, like that corresponding to the inviscid bubble, and only a small effect of Ac on C_{VD} is observed. Asymmetry increases with Re and the modification of surface vorticity by the strain is very different from the behaviour depicted by (35) and results in a much more significant effect. Correlation (39*b*) obtained for $Re_0 \geqslant 10$ shows a severe modification of the viscous drag by the strain related in particular to the changes of size of the separated region. A contribution $0.57Ac$ which has the form of an inertial term appear in (39*b*) and traduces an important variation of C_{VD} with Ac. Since the term $0.57Ac$ has been obtained through a fitting procedure limited to $Re \leqslant 300$ it cannot be concluded that it represents really an effect of inertia and still exists at very high values of Re where viscous effects become asymptotically small. Present results just show that the modification of the viscous drag of a rigid sphere by the strain cannot be ignored at Reynolds numbers of several hundreds: in our simulations the variation of the total drag coefficient C_D linked to this effect goes from 4% at $Re_0 = 0.1$ to 22% at $Re_0 = 300$ for $Ac = 0.2$.

The contribution $0.57Ac$ found in the correlation (39*b*) has the same order of magnitude as that linked to the added mass force ($0.667Ac$). Thus both must be taken into account in practical calculations of particles trajectories. However, it must be stressed that the nature of the two effects is fundamentally different and that no conclusion can be drawn from the term $0.57Ac$ concerning the evolution of C_{VD} with Ac for values of Re_0 larger than those explored in the present simulations. It is unfortunately not possible to develop general analytical expressions for the modification of the viscous drag produced by the strain. For practical calculations it is highly desirable to get correlations giving directly the drag coefficient C_{Dm} taking into account this effect (without any splitting between viscous and pressure contributions) in terms of the drag coefficient in uniform flow. Since (1) was shown to

be valid for viscous flows, the total force experienced by a spherical particle at rest in a steady straining flow can be expressed as

$$\boldsymbol{F} = \tfrac{1}{8}C_{Dm}(Re_0, Ac)\,\pi D^2\rho|\boldsymbol{V}|\,\boldsymbol{V} + \rho\mathscr{V}(1+C_M)\,\boldsymbol{V}\cdot\boldsymbol{\nabla}\boldsymbol{V}. \tag{43}$$

Keeping in mind that the averaged error on the drag coefficients can be estimated as 0.01 (i.e. $0.05Ac$ when $|Ac| = 0.2$) the results reported in tables 1–4 lead to the following approximate relations between C_{Dm} and C_D for $10 \leqslant Re_0 \leqslant 300$:

$$C_{Dm}(Re_0, Ac) = (1+0.25Ac)\,C_D(Re_0, 0) + 0.55Ac \quad \text{for the rigid sphere,} \tag{44a}$$

$$C_{Dm}(Re_0, Ac) = C_D(Re_0, 0) \quad \text{for the inviscid bubble.} \tag{44b}$$

4.7. *The history force in non-uniform flows*

We have previously shown that computing the flow around a fixed sphere embedded in a pure straining flow allows one to find the correct generalization of the time derivative $\partial\boldsymbol{V}/\partial t$ which must be used in the expression for the added mass force for non-uniform flows: this generalization is the acceleration of the fluid, i.e. $\mathrm{D}\boldsymbol{V}/\mathrm{D}t = \partial\boldsymbol{V}/\partial t + \boldsymbol{V}\cdot\boldsymbol{\nabla}\boldsymbol{V}$, and not the derivative of $\boldsymbol{V}$ following the particle, i.e. $\mathrm{d}\boldsymbol{V}/\mathrm{d}t = \partial\boldsymbol{V}/\partial t + \boldsymbol{V}_P\cdot\boldsymbol{\nabla}\boldsymbol{V}$. A similar unsolved question exists concerning the history force. Unfortunately it cannot be answered by considering either inviscid flows (since no history force exists in this case) or creeping flows since $\mathrm{D}\boldsymbol{V}/\mathrm{D}t$ and $\mathrm{d}\boldsymbol{V}/\mathrm{d}t$ are indistinguishable for $Re \ll 1$ (Maxey & Riley 1983). Drew & Wallis (1992) suggested a solution by assuming that the history force must be frame indifferent. When the unperturbed flow is irrotational their argument leads to choosing $\mathrm{D}\boldsymbol{V}/\mathrm{D}t$ as the correct generalization. The steady straining flow considered here suggests a very simple way to check the various proposals and finally get the right expression on purely physical grounds.

Let us suppose that the history force experienced by a rigid sphere be given in uniform flow by the classical expression found by Boussinesq (1885) and Basset (1888):

$$\boldsymbol{F}_H = \tfrac{3}{2}D^2(\pi\mu\rho)^{1/2}\int_{t_0}^{t}\frac{\partial\boldsymbol{V}/\partial\tau - \boldsymbol{a}_P(\tau)}{(t-\tau)^{1/2}}\,\mathrm{d}\tau. \tag{45}$$

Let us now suppose that the correct generalization for non-uniform flows of the term $\partial\boldsymbol{V}/\partial\tau = \{\partial\boldsymbol{V}/\partial t\}_{t=\tau}$ be $\{\mathrm{D}\boldsymbol{V}/\mathrm{D}t\}_{t=\tau,\,x=x_0(\tau)}$, $\boldsymbol{x}_0$ standing for the instantaneous position of the centre of the sphere. The history force experienced by a sphere at rest in the straining flow defined by (31*a*, *b*) can then be obtained by evaluating (45) on replacing $\partial\boldsymbol{V}/\partial\tau$ by $\{\mathrm{D}\boldsymbol{V}/\mathrm{D}t\}_{t=\tau,\,x=x_0(\tau)}$. The result is a non-zero force $\boldsymbol{F}_H = 3\alpha V_0\,D^2(\pi\mu\rho(t-t_0))^{1/2}\,\boldsymbol{e}_z$. This is evidently not correct: time plays no role in a situation where the flow is steady and the body does not move. Consequently the history force is necessarily zero. It can be concluded from this conflict that no term of the form $\boldsymbol{V}\cdot\boldsymbol{\nabla}\boldsymbol{V}$ can be involved in the proper generalization of $\partial\boldsymbol{V}/\partial\tau$. In contrast, since $\boldsymbol{V}_P = \boldsymbol{0}$, a generalization involving the derivative of $\boldsymbol{V}$ following the sphere $\{\mathrm{d}\boldsymbol{V}/\mathrm{d}t\}_{t=\tau,\,x=x_0(\tau)}$ leads to the correct result $\boldsymbol{F}_H = \boldsymbol{0}$. This proposal is the unique correct answer to the problem as can be demonstrated by considering the same physical situation in a frame of reference $\mathscr{R}'$ moving with an arbitrary constant velocity $\boldsymbol{c} = c\boldsymbol{e}_z$. In $\mathscr{R}'$ the coordinates transform as $\boldsymbol{x}' = \boldsymbol{x} - ct\boldsymbol{e}_z$, $t' = t$ and the unperturbed streamwise fluid velocity corresponding to (31*a*) is given by $V_z'(z', t') = V_0 - c + \alpha(z' + ct')$. Thus in $\mathscr{R}'$ the flow is no longer steady and we get $\partial'\boldsymbol{V}'/\partial t' = \alpha c\boldsymbol{e}_z = \boldsymbol{c}\cdot\boldsymbol{\nabla}'\boldsymbol{V}'$ ($\partial'/\partial t'$ and $\boldsymbol{\nabla}'$ denoting the operators evaluated in $\mathscr{R}'$). It is well known from the principle of Galilean invariance that the history force, like the other forces, must remain the same in any Galilean frame of reference. Consequently, to maintain $\boldsymbol{F}_H = \boldsymbol{0}$ in $\mathscr{R}'$ the correct generalization of $\partial\boldsymbol{V}/\partial\tau$

written in $\mathscr{R}'$ must be in the present case $\{\partial' V'/\partial t' - \boldsymbol{c}\cdot\boldsymbol{\nabla}' V'\}_{t=\tau,\, x=x_0(\tau)}$. Since $V_P = \mathbf{0}$ this is nothing other than $\{\mathrm{d}' V'/\mathrm{d}t'\}_{t=\tau,\, x=x_0(\tau)}$. So by combining a physical situation where $\mathrm{d}V/\mathrm{d}t = \mathbf{0}$ while $\mathrm{D}V/\mathrm{D}t \neq \mathbf{0}$ with the principle of Galilean invariance we have demonstrated that $\{\mathrm{d}V/\mathrm{d}t\}_{t=\tau,\, x=x_0(\tau)}$ is the proper generalization of $\partial V/\partial\tau$ to be used for the history force in non-uniform flows. Note that if we now consider the case where the sphere moves with a constant velocity $V_P = V_P \boldsymbol{e}_z$ in the same straining flow we get, using $\{\mathrm{d}V/\mathrm{d}t\}_{t=\tau,\, x=x_0(\tau)}$ in place of $\partial V/\partial\tau$ in (45): $\boldsymbol{F}_H = 3\alpha V_P D^2(\pi\mu\rho(t-t_0))^{1/2}\boldsymbol{e}_z$. The existence of a non-zero history force in that case is not unlikely since as the sphere moves it sees a varying fluid velocity.

From the foregoing discussion we can conclude that the correct generalization of $\partial V/\partial t$ to be used in non-uniform flows is not the same in the added mass term and in the history force: added mass involves the acceleration of the fluid while history force involves the derivative of the fluid velocity following the particle. Furthermore this discussion shows that use of the principle of frame indifference to determine the list of vectorial or tensorial arguments which can enter into the expression of the various hydrodynamic forces (Drew & Lahey 1979; Drew & Wallis 1992) leads in the present case to erroneous conclusions. Thus we may conclude that frame indifference cannot be retained as a general guiding principle as soon as inertia effects (i.e. non-zero relative Reynolds numbers) are considered.

5. Conclusions

In this paper we have reported some results of a numerical investigation of two steady axisymmetric flows around a sphere, namely the uniform flow and the pure straining flow. The numerical code developed for this study uses a velocity–pressure formulation combined with a finite-volume discretization of the Navier–Stokes equations written in general orthogonal coordinates. Computations have been carried out in the range $0.1 \leqslant Re \leqslant 300$ in order to cover roughly all the laminar regime. Since we are interested in both particle-laden and bubbly flows a systematic comparison between flows around a rigid sphere and those around an inviscid spherical bubble has been pursued. The study of the pure straining flow has yielded several important results:

(i) The presence of the strain modifies deeply the distribution of vorticity around the sphere. This modification originates in two different mechanisms. On the one hand, compared to uniform flow, the viscous boundary condition (no-slip or shear-free) that must be satisfied by the straining flow on the sphere induces an additional contribution to surface vorticity. On the other hand the streamlines of the basic flow are curved and force the vorticity field to follow a specific spatial distribution.

(ii) These modifications have no spectacular consequences in the case of an inviscid bubble since no separation occurs. In contrast the characteristics of the flow near the rigid sphere are greatly modified: in the case of a positive strain the recirculating region first appears at a higher value of Re_0 than in uniform flow. Moreover the separation angle and the reattachment length are strongly reduced.

(iii) A specific vortex-stretching mechanism due to the combination of axisymmetry and straining exists in this type of flow. When Ac is positive this mechanism acts to reduce the extent of the region where vorticity is significant. In contrast when Ac is negative the same mechanism leads (in the inviscid limit) to a discontinuity of both the velocity and the vorticity across the stagnation plane. This specific feature provides the basis of an instability of the steady biaxial straining flow which occurs for each value of Ac when Re_0 increases beyond a critical value.

(iv) Computations of the total drag force have shown that the sphere undergoes an added mass force in this purely steady situation with the sphere at rest. This proves that the concept of added mass holds for viscous non-uniform flows and that the added mass force involves the acceleration of the fluid DV/Dt. Furthermore our results show that the added mass coefficient remains the same as in inviscid flow or in creeping flow, i.e. $C_M = \frac{1}{2}$, whatever the Reynolds number in the range covered by the present computations.

(v) Changes found in vorticity distribution are reflected in the viscous drag: compared to uniform flow the viscous drag is increased by a positive strain and decreased by a negative one. For the inviscid bubble the overall effect is a small modification which can generally be ignored in practical calculations. In contrast, for the rigid sphere the effect increases with Re_0 and goes beyond 10% for $Re_0 \geqslant 100$.

(vi) Finally, physical reasoning has shown that in non-uniform flows, the time derivative of the fluid velocity V involved by the history force must be generalized by using the derivative of V following the particle.

We thank D. Legendre for improving numerous computations discussed in this paper and providing several new results. Computations have been carried out on the IMB 3090/600VF of the Centre National Universitaire Sud de Calcul in Montpellier with the support of the 'Centre de Compétences en Calcul Numérique Intensif'.

REFERENCES

ACHENBACH, E. 1974 Vortex shedding from spheres. *J. Fluid Mech.* **62**, 209.

AMSDEN, A. & HARLOW, F. 1972 The SMAC Method: A numerical technique for calculating incompressible fluid flow. *Los Alamos Res. Lab. Rep.* LA-4370.

AUTON, T. R., HUNT, J. C. R. & PRUD'HOMME, M. 1988 The force exerted on a body in inviscid unsteady non-uniform rotational flow. *J. Fluid Mech.* **197**, 241.

BASSET, A. B. 1888 *A treatise in Hydrodynamics*, vol. 2. Cambridge: Deighton Bell.

BATAILLE, J., LANCE, M. & MARIÉ, J. L. 1990 Some aspect of the modeling of bubbly flows. In *Phase–Interface Phenomena in Multiphase Flow* (ed. G. F. Hewitt, F. Mayinger & J. R. Riznic). Hemisphere.

BATCHELOR, G. K. 1967 *An introduction to Fluid Dynamics*. Cambridge University Press.

BOUSSINESQ, J. 1885 Sur la résistance qu'oppose un fluide indéfini au repos, sans pesanteur, au mouvement varié d'une sphère solide qu'il mouille sur toute sa surface, quand les vitesses restent bien continues et assez faibles pour que leurs carrés et produits soient négligeables. *C. R. Acad. Sci. Paris* **100**, 935.

BRABSTON, D. C. & KELLER, H. B. 1975 Viscous flows past spherical gas bubbles. *J. Fluid Mech.* **69**, 179.

BRAÎLOVSKAYA, I. Y. 1965 A difference scheme for numerical solution of the two-dimensional nonstationary Navier–Stokes equations for a compressible gas. *Sov. Phys. Dokl.* **10**, 107.

CLIFT, R., GRACE, J. R. & WEBER, M. E. 1978 *Bubbles, Drops and Particles*. Academic Press.

CONNER, J. M. & ELGOBASHI, S. E. 1987 Numerical solution of laminar flow past a sphere with surface mass transfer. *Num. Heat Transfer* **12**, 57.

DARWIN, C. 1953 Note on hydrodynamics. *Camb. Phil. Trans.* **49**, 342.

DENNIS, S. C. R. & WALKER, J. D. A. 1971 Calculation of the steady flow past a sphere at low and moderate Reynolds numbers. *J. Fluid Mech.* **48**, 771.

DREW, D. A. & LAHEY, R. T. 1979 Application of general constitutive principles to the derivation of multidimensional two-phase flows equations. *Intl J. Multiphase Flow* **5**, 243.

DREW, D. A. & WALLIS, G. B. 1992 Fundamentals of two-phase flow modeling. *Symp. Two-Phase Flow Modelling, London* (unpublished).

FORNBERG, B. 1988 Steady viscous flow past a sphere at high Reynolds number. *J. Fluid Mech.* **190**, 471.

GALPIN, P. F. & RAITHBY, G. D. 1986 Treatment of non-linearities in the numerical solution of the incompressible Navier–Stokes equations. *Intl J. Num. Meth. Fluids* **6**, 409.

GATIGNOL, R. 1983 The Faxén formulae for a rigid particle in an unsteady non-uniform Stokes flow. *J. Méc. Théor. Appl.* **1**, 143.

HADAMARD, J. S. 1911 Mouvement permanent lent d'une sphère liquide et visqueuse dans un liquide visqueux. *C.R. Acad. Sci. Paris* **152**, 1735.

HARLOW, F. H. & WELCH, J. E. 1965 Numerical calculation of time-dependent viscous incompressible flow of fluid with free surface. *Phys. Fluids* **8**, 2182.

KANG, I. S. & LEAL, L. G. 1987 Numerical solution of axisymmetric, unsteady free-boundary problems at finite Reynolds number. I. Finite-difference scheme and its application to the deformation of a bubble in a uniaxial straining flow. *Phys. Fluids* **30**, 1929.

KANG, I. S. & LEAL, L. G. 1988 The drag coefficient for a spherical bubble in a uniform streaming flow. *Phys. Fluids* **31**, 233.

KANG, I. S. & LEAL, L. G. 1989 Numerical solution of axisymmetric, unsteady free-boundary problems at finite Reynolds number. II. Deformation of a bubble in biaxial straining flow. *Phys. Fluids* A **1**, 644.

KIM, I. & PEARLSTEIN, A. J. 1990 Stability of the flow past a sphere. *J. Fluid Mech.* **211**, 73.

LAMB, H. 1932 *Hydrodynamics*, 6th edn. Cambridge University Press.

LE CLAIR, B. P., HAMIELEC, A. E. & PRUPPACHER, H. E. 1970 A numerical study of the drag of a sphere at low and intermediate Reynolds numbers. *J. Atmos. Sci.* **27**, 308.

LEAL, G. 1989 Vorticity transport and wake structure for bluff bodies at finite Reynolds number. *Phys. Fluids* A **1**, 124.

LEVICH, V. G. 1949 Bubble motion at high Reynolds numbers *Zh. Eksp. Teoret. Fiz.* **19**, 18 (in Russian).

LEVICH, V. G. 1962 *Physicochemical Hydrodynamics*. Prentice Hall.

LHUILLIER, D. 1982 Forces d'inertie sur une bulle en expansion se déplaçant dans un fluide. *C.R. Acad. Sci. Paris* **295**(II), 95.

MAGNAUDET, J., RIVERO, M., LEGENDRE, D. & FABRE, J. 1995 Accelerated flows past a rigid sphere or a spherical bubble. Part 2. Uniform unsteady flows. *J. Fluid Mech.* (to be submitted).

MAXEY, M. R. & RILEY, J. J. 1983 Equation of motion for a small rigid sphere in a non-uniform flows. *Phys. Fluids* **26**, 883.

MOIN, P. & KIM, J. 1985 Application of a fractional-step method to incompressible Navier–Stokes equations. *J. Comput. Phys.* **59**, 308.

MOORE, D. W. 1963 The boundary layer on a spherical gas bubble. *J. Fluid Mech.* **16**, 161.

NACIRI, A. 1992 Contribution à l'étude des forces exercées par un liquide sur une bulle de gaz: portance, masse ajoutée et interactions hydrodynamiques. Thèse de Doctorat, Ec. Centrale de Lyon.

NATARAJAN, R. & ACRIVOS, A. 1993 The instability of the steady flow past spheres and disks. *J. Fluid Mech.* **254**, 323.

OLIVER, D. L. R. & CHUNG, I. N. 1987 Flow about a sphere at low to moderate Reynolds numbers. *J. Fluid Mech.* **177**, 1.

PEYRET, R. & TAYLOR, T. 1983 *Computational Methods for Fluid Flow*. Springer.

POPE, S. B. 1978 The calculation of turbulent recirculating flows in general orthogonal coordinates. *J. Comput. Phys.* **26**, 197.

PROUDMAN, I. & PEARSON, J. R. A. 1957 Expansions at small Reynolds for the flow past a sphere and a circular cylinder. *J. Fluid Mech.* **2**, 237.

PRUPPACHER, H. R., LE CLAIR, B. P. & HAMILIEC, A. E. 1970 Some relations between drag and flow pattern of viscous flow past a sphere and a cylinder at low and intermediate Reynolds numbers. *J. Fluid Mech.* **44**, 781.

RALLISON, J. M. 1984 The deformation of small viscous drops and bubbles in shear flows. *Ann. Rev. Fluid Mech.* **16**, 45.

RIBCZYNSKI, W. 1911 On the translatory motion of a fluid sphere in a viscous medium. *Bull. Intl Acad. Pol. Sci. Lett.: Sci. Math. Nat.* (A), 40 (in German).

RIMON, Y. & CHENG, I. 1969 Numerical solution of a uniform flow over a sphere at intermediate Reynolds numbers. *Phys. Fluids* **12**, 949.

RIVERO, M. 1991 Etude par simulation numérique des forces exercées sur une inclusion sphérique par un écoulement accéléré. Thèse de Doctorat, Inst. Polytech. de Toulouse.

RYSKIN, G. & LEAL, L. G. 1984*a* Numerical solution of free boundary problems in fluid mechanics. Part 1. The finite difference technique. *J. Fluid Mech.* **148**, 1.

RYSKIN, G. & LEAL, L. G. 1984*b* Numerical solution of free boundary problems in fluid mechanics. Part 3. Uniaxial straining flow. *J. Fluid Mech.* **148**, 37.

RYVKIND, V. Y. & RYSKIN, G. 1976 Flow structure in motion of a spherical drop in a fluid medium at intermediate Reynolds number. *Fluid Dyn.* **11**, 5.

SAKAMOTO, H. & HANIU, H. 1990 A study of vortex shedding from spheres in a uniform flow. *Trans. ASME* I: *J. Fluids Engng* **112**, 386.

STOKES, G. G. 1851 On the effect of the internal friction of fluids on the motion of pendulums. *Trans. Camb. Phil. Soc.* **9**, 8.

TANEDA, S. 1956 Studies on wake vortices (III). Experimental investigation of the wake behind a sphere at low Reynolds numbers. *J. Phys. Soc. Japan* **11**, 1104.

TAYLOR, G. I. 1928 The forces on a body placed in a curved or converging stream of fluid. *Proc. R. Soc. Lond.* A **120**, 260.

TAYLOR, T. D. & ACRIVOS, A. 1964 On the deformation and drag of a falling viscous drop at low Reynolds number. *J. Fluid Mech.* **18**, 466.

TCHEN, C. M. 1947 Mean value and correlation problems connected with the motion of small particles suspended in a turbulent fluid. PhD dissertation, Technische Hogeschool Delft.

TOLLMIEN, W. 1938 Uber krafte und momente in schwach gekrummten oder konvergenten stromungen. *Ing.-Arch.* **9**, 308.

VOINOV, V. V., VOINOV, O. V. & PETROV, A. G. 1973 Hydrodynamic interactions between bodies in a perfect incompressible fluid and their motion in non-uniform streams. *Prikl. Math. Mekh.* **37**, 680.